

Evidence for Realignment of the Charge Density Wave State in ErTe_3 and TmTe_3 under Uniaxial Stress via Elastocaloric and Elastoresistivity Measurements

J. A. W. Straquadine^{1,2,*}, M. S. Ikeda, and I. R. Fisher

*Geballe Laboratory for Advanced Materials and Department of Applied Physics,
Stanford University, Stanford, California 94305, USA
and Stanford Institute for Materials and Energy Sciences, SLAC National Accelerator Laboratory,
2575 Sand Hill Road, Menlo Park, California 94025, USA*

 (Received 7 January 2022; revised 13 March 2022; accepted 15 April 2022; published 26 May 2022)

We report the evolution of the charge density wave (CDW) states in the quasi-two-dimensional rare-earth tritellurides ($R\text{Te}_3$ for $R = \text{Er}, \text{Tm}$) under the influence of in-plane uniaxial stress. Measurements of the elastocaloric effect, resistivity, and elastoresistivity allow us to demonstrate the importance of in-plane antisymmetric strain on the CDW and to establish a phase diagram. We show that modest tensile stress parallel to the in-plane a axis can reversibly switch the direction of the ordering wave vector between the two in-plane directions, and present a free-energy expansion which reproduces the general structure of the observed phenomena. This work opens a new avenue in the study of $R\text{Te}_3$ in its own right, and more generally establishes $R\text{Te}_3$ as a promising model system for the study of strain-CDW interactions in a quasi-two-dimensional square lattice.

DOI: [10.1103/PhysRevX.12.021046](https://doi.org/10.1103/PhysRevX.12.021046)

Subject Areas: Condensed Matter Physics
Strongly Correlated Materials

I. INTRODUCTION

The family of rare-earth tritelluride materials ($R\text{Te}_3$, $R = \text{La-Nd}, \text{Sm}, \text{Gd-Tm}, \text{Y}$) has been studied for decades [1,2] as a model system for unidirectional charge density wave (CDW) formation in quasi-two-dimensional metals with an almost square lattice. Recent studies [3–5] have pointed out the inadequacy of the original picture of a nesting-driven [1,2,6], Peierls-like CDW transition. The simple and well-understood electronic structure, weak electronic correlations, and absence of strong magnetic fluctuations all make $R\text{Te}_3$ a promising system to improve understanding of the origins and consequences of non-Peierls CDW ordered states.

While the mechanisms driving CDW formation can be material dependent [5,7–10], there is an overarching consensus that strong coupling between the electronic and lattice degrees of freedom is crucial [3]. As such, modifying the lattice with hydrostatic pressure, chemical pressure, or uniaxial stress can produce substantial changes in the CDW state [11–16]. The response of the CDW to such

perturbations contains a wealth of information about the host material, ordered state, and the phase transition.

In this paper, we report investigations of the effect of in-plane uniaxial stress on unidirectional CDW states in ErTe_3 and TmTe_3 . We provide evidence of in-plane realignment of the CDW wave vector under modest and practically accessible stresses. It appears that the weak orthorhombicity acts as a bias “field” on the direction of the CDW, and that suitable uniaxial stress can overcome this bias and reverse the anisotropy of the CDW gap. Through this comprehensive study of the phases and phase transitions, we determine a stress-temperature phase diagram and establish $R\text{Te}_3$ as a promising model system for the study of strain-CDW interactions in a quasi-2D square lattice.

Unidirectional CDW states break both translational and rotational symmetries. The rotational component of the electronic order parameter will couple strongly to externally induced strains which break the same symmetry. However, the situation becomes less clear in the presence of disorder or competing instabilities [17–20], as in the case of CDW order in the cuprate superconductors [21–25]. The interplay between the CDW and superconducting states in those materials is currently a subject of debate. To the extent that the CDW phenomena can be reproduced and studied in structurally similar, yet physically simpler materials, one can endeavor to improve understanding of the role played by charge order by means of analogy. $R\text{Te}_3$ is regarded as a model system for unidirectional CDW formation, but the evolution of the CDW under in-plane, uniaxial stress has not

*jstraq@stanford.edu

Published by the American Physical Society under the terms of the [Creative Commons Attribution 4.0 International license](https://creativecommons.org/licenses/by/4.0/). Further distribution of this work must maintain attribution to the author(s) and the published article's title, journal citation, and DOI.

been evaluated. This article opens a previously unexplored avenue of study into CDW formation in $R\text{Te}_3$ by introducing uniaxial stress as a tuning parameter.

We employ two uniaxial-stress techniques, namely, the elastocaloric effect (ECE) and the elastoresistivity (ER), to elucidate the phase diagram of $R\text{Te}_3$. The elastocaloric effect is a thermodynamic probe which measures the effects of strain on the entropy landscape. ECE measurements mimic the singular behavior at a phase transition observed in heat capacity C_p , but the selective sensitivity of ECE only to strain-dependent degrees of freedom leads to a much lower background signal at high temperatures than C_p [26]. In contrast, elastoresistivity is a transport probe that is sensitive to strain-induced changes in the Fermi surface (FS) topology, density of states at the Fermi surface, and scattering processes such as critical fluctuations.

Members of the rare-earth tritelluride family consist of bilayers of square Te nets separated by a buckled rocksalt layer of $R\text{Te}$, shown in Fig. 1(a). The crystal structure of $R\text{Te}_3$ belongs to the orthorhombic space group $Cmcm$, and the standard crystallographic setting defines the b axis normal to the planes. The orthorhombicity arises due to a glide plane along the in-plane c axis, which dictates the stacking of the $R\text{Te}$ slab layers and generates a slight difference in the two in-plane lattice parameters: $a \approx 0.999c$; hence, this material comprises an ‘‘almost square’’ lattice. For all R , the material undergoes a transition to a unidirectional, incommensurate CDW phase with the wave vector $q_c \approx (0, 0, 2c^*/7)$, where c^* is the reciprocal lattice spacing. Chemical pressure tunes the transition temperature from above 500 K in LaTe_3 to 250 K in TmTe_3 . A second incommensurate CDW perpendicular to the first, with wave vector $q_a \approx (5a^*/7, 0, 0)$, appears for $R = \text{Tb}, \text{Dy}, \text{Ho}, \text{Er}, \text{Tm}$ at temperatures ranging from 41 K in TbTe_3 [27] to 180 K in TmTe_3 . Throughout this work, we denote the higher transition temperature as T_{CDW1} and the lower transition as T_{CDW2} . In freestanding samples, T_{CDW1} corresponds to a wave vector parallel to the c axis.

We begin in Sec. II by developing a phenomenological, symmetry-motivated free-energy expansion and exploring the resulting phase diagrams. Section III covers the experimental methods, and Sec. IV describes the results of elastocaloric effect, resistivity, and elastoresistivity measurements. We conclude in Sec. V with a discussion of the broader impacts and future research opportunities inspired by this work.

II. UNIDIRECTIONAL CDWs IN A QUASITETRAGONAL SYSTEM

Before describing our results in this specific model system, it is instructive to consider the general expectations for the free-energy and the phase diagram. Consider a two-dimensional system with tetragonal symmetry which supports incommensurate unidirectional CDW order along

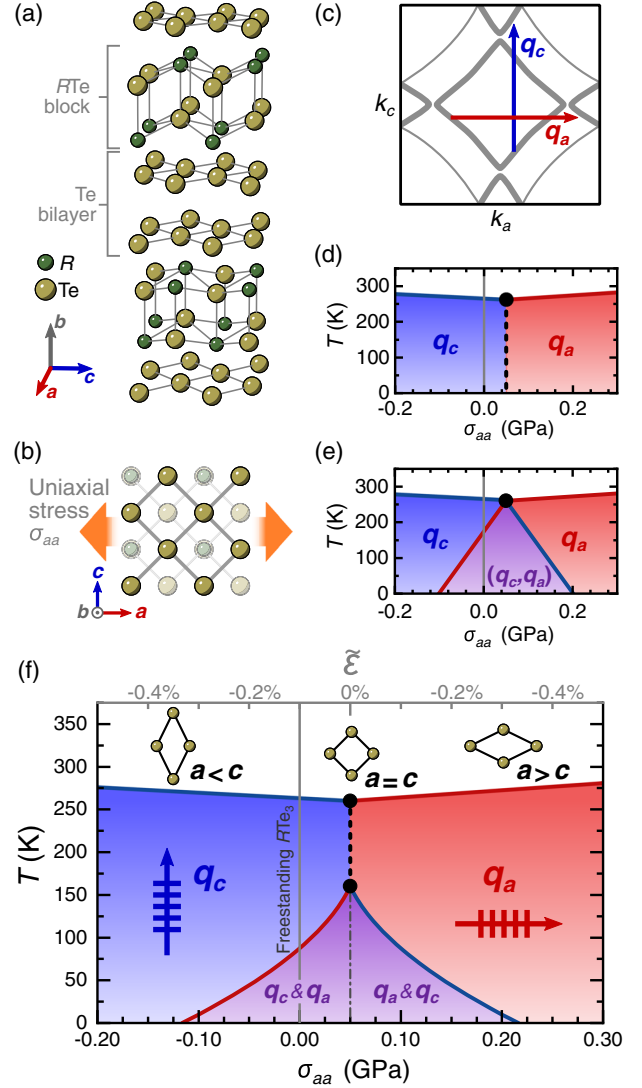


FIG. 1. (a) Crystal structure of $R\text{Te}_3$. The stacking of the $R\text{Te}$ block layers produces a glide plane which breaks C_4 symmetry. (b) Crystal structure viewed along the out-of-plane b axis. Tensile stress along the a axis can invert the native orthorhombic distortion, $a \approx 0.999c$. (c) Schematic of the Fermi surface of $R\text{Te}_3$, neglecting the small b -axis dispersion and bilayer splitting. (d) Temperature-uniaxial stress phase diagram described by Eq. (2) for $g > 0$. Solid lines indicate continuous phase transitions, and dashed lines indicate first-order transitions. The stress axis is defined relative to a freestanding orthorhombic $R\text{Te}_3$ crystal. (e) Phase diagram of Eq. (2) for $g < 0$. A region of coexisting CDW order with both wave vectors opens at low temperatures, and all transitions are continuous. (f) Phase diagram of Eq. (6) incorporating higher-order terms, which preserves the first-order transition (between multicritical points) and the coexistence region. While missing from this model, resistivity measurements (Sec. IV B) suggest the first-order transition persists to lower temperature as well (dash-dotted line). Coefficients appropriate for ErTe_3 are used in calculating (d)–(f).

both the a and c axes, where we keep the notation of a and c as in-plane lattice parameters for immediate comparison to $R\text{Te}_3$.

Following the seminal work of McMillan [28], but using the crystallographic coordinates of $R\text{Te}_3$, we take as our order parameters

$$\psi_j(\mathbf{r}) = \psi_{j0}(\mathbf{r})e^{i\mathbf{q}_j \cdot \mathbf{r}}, \quad (1)$$

where $j = a, c$, and the subscript 0 is used to indicate the absence of applied stress.

Knowledge of the $R\text{Te}_3$ family allows us to make several simplifying assumptions. The absence of commensurability effects (suggested by the smooth variation of \mathbf{q}_c and \mathbf{q}_a with temperature [27,29,30]) coupled with the low levels of CDW-pinning disorder (as observed in x-ray diffraction [27,30], STM [31–33], electrical transport [34,35], and quantum oscillations [15,36,37]) allows us to treat the wave vectors \mathbf{q}_a and \mathbf{q}_c as fixed, spatially uniform parameters. Also, as the two wave vectors are not parallel, the phases of the order parameters $\psi_a(\mathbf{r})$ and $\psi_c(\mathbf{r})$ are mutually independent. These assumptions together allow us to consider only the CDW gap magnitudes and suppress any gradient terms in our free-energy expansion. For brevity, from this point forward we use the notation $\psi_a = |\psi_a|$, $\psi_c = |\psi_c|$.

To introduce stress and strain terms into our free energy, we must also make a distinction between this idealized tetragonal model and the realistic orthorhombic structure of $R\text{Te}_3$. The stress and strain tensors in these two cases can be captured by a weakly temperature-dependent offset: $\varepsilon_{ij} + \varepsilon_{ij}^0 = \tilde{\varepsilon}_{ij}$, $\sigma_{ij} + \sigma_{ij}^0 = \tilde{\sigma}_{ij}$, where a tilde denotes the tetragonal case [38].

Furthermore, we choose a basis for the stress, strain, and elastic constant tensors motivated by tetragonal symmetry. We use subscripts A and S for antisymmetric and symmetric in-plane components, respectively: $\tilde{\varepsilon}_A = (\tilde{\varepsilon}_{cc} - \tilde{\varepsilon}_{aa})/2$, $\tilde{\varepsilon}_S = (\tilde{\varepsilon}_{cc} + \tilde{\varepsilon}_{aa})/2$, and similar for the stresses $\tilde{\sigma}_A$ and $\tilde{\sigma}_S$ [39]. In this basis and neglecting out-of-plane contributions, the symmetrized and antisymmetrized elastic constants are defined as $\tilde{C}_S \approx C_S = 2(C_{aaaa} + C_{aacc})$ and $\tilde{C}_A \approx C_A = 2(C_{aaaa} - C_{aacc})$, where the factor of 2 is added for convenience.

Taking the tetragonal case as a reference, consider an expansion to fourth order in ψ_a and ψ_c of the Gibbs free energy (constant stress, constant temperature) given by

$$G_4 = G_\psi + G_\varepsilon + G_c, \quad (2)$$

$$G_\psi = \frac{a_0 t}{2}(\psi_a^2 + \psi_c^2) + \frac{b}{4}(\psi_a^2 + \psi_c^2)^2 + \frac{g}{2}\psi_a^2\psi_c^2, \quad (3)$$

$$G_\varepsilon = \frac{\tilde{C}_A}{2}\tilde{\varepsilon}_A^2 + \frac{\tilde{C}_S}{2}\tilde{\varepsilon}_S^2 - 2(\tilde{\sigma}_A\tilde{\varepsilon}_A + \tilde{\sigma}_S\tilde{\varepsilon}_S), \quad (4)$$

$$G_c = \lambda\tilde{\varepsilon}_A(\psi_c^2 - \psi_a^2) + \eta\tilde{\varepsilon}_S(\psi_c^2 + \psi_a^2), \quad (5)$$

where $t = (T - T_c^0)/T_c^0$ is the reduced temperature and T_c^0 is the critical temperature in the hypothetical tetragonal

crystal. Translational symmetry prevents the existence of bilinear terms involving the order parameters; the λ and η terms are the lowest-order strain couplings allowed. The coefficients a_0, b as well as the elastic constants C_S and C_A must be positive for stability. Empirically, the antisymmetric coupling constant λ must be negative to stabilize the CDW parallel to the longer in-plane c axis. This is also supported by measurements of the thermal expansion below T_{CDW1} [30]. Hydrostatic pressure experiments [11,14,15] suggest that the symmetric coupling coefficient η must also be negative. The orthorhombic crystal structure implies that the lowest-order couplings between the order parameters and shear strains ε_{ab} , ε_{bc} , and ε_{ac} are biquadratic and are neglected here.

Previous work has explored the $R\text{Te}_3$ phase diagram with the assumption of C_4 symmetry without strain coupling [40], equivalent to the case $\lambda = \eta = 0$. In this case, g must be positive in order for a unidirectional CDW to form rather than a checkerboard state. In this case, finite strain coupling “selects” the CDW wave vector between the \mathbf{q}_c and \mathbf{q}_a states, separated by a first-order transition as shown in Fig. 1(d). In such a model, no second CDW transition is observed at lower temperatures. This would appropriately describe the phase diagram of $R\text{Te}_3$ for $R = \text{La}, \text{Ce}, \text{Pr}, \text{Nd}, \text{Sm}, \text{and Gd}$.

The case for $g < 0$, considered in Fig. 1(e), exhibits similar wave vector switching behavior but with a region of coexisting \mathbf{q}_c and \mathbf{q}_a states, bounded by a pair of second-order transitions. At first glance, a vertical cut of this phase diagram for finite $\tilde{\sigma}_A$ appears to reproduce the cascade of phase transitions observed in $R\text{Te}_3$ for $R = \text{Tb}, \text{Dy}, \text{Ho}, \text{Er}, \text{and Tm}$.

The measurements reported in Secs. IV A, IV B, and IV D all suggest, however, that the real phase diagram exhibits both a first-order transition and a coexistence region; therefore neither of these two phase diagrams is sufficient. The phase diagram for the heavy rare-earth compounds therefore requires the inclusion of higher-order terms. One such model has been explored to eighth order for the case of $R\text{Te}_3$ in the presence of disorder [41]. In the pristine case, we have found that adding the two possible sixth-order terms Eq. (2) suffices to capture the basic phenomenology of our observations:

$$G = G_4 + r(\psi_c^2 + \psi_a^2)^3 + \gamma(\psi_c^4\psi_a^2 + \psi_c^2\psi_a^4), \quad (6)$$

where $g > 0$, $r > 0$, and $\gamma \approx -r/2$. This phase diagram is shown in Fig. 1(f). Comparing our results to the physically distinct cases presented in Figs. 1(d)–1(f) will provide insight into the nature of the CDW states and their mutual interactions. The experimental results described through the rest of this article will demonstrate that the stress-temperature phase diagram of $R\text{Te}_3$ incorporates a first-order transition as well as two independent CDW

transitions, and therefore matches the structure of Fig. 1(f) more closely than Fig. 1(d) or Fig. 1(e).

III. EXPERIMENTAL METHODS

Single crystals of ErTe_3 and TmTe_3 are grown by a self-flux method described elsewhere [34]. Further details of sample mounting, contacts, and thermometry can be found in the Appendix A.

Uniaxial stress was generated using a commercially available stress cell, specifically the CS-100 from Razorbill Instruments, in which a bar-shaped sample was suspended between a pair of mounting plates. The sample was then stressed by changing the spacing of the mounting plates *in situ* by applying voltages to three piezoelectric actuators [stacks of lead zirconate titanate (PZT)] shown schematically in Fig. 2. Two independent control voltages, V_{inner} and V_{outer} , were applied to the inner and outer PZT stacks, respectively. $V_{\text{outer}} > 0$ induced tensile stress in the sample and $V_{\text{inner}} > 0$ induced compressive stress.

Measurements of ECE and ER require the superposition of both static and oscillating stresses. Signals of the form $V_{\text{outer}} = V_{\text{dc}} + V_{\text{ac}} \cos(2\pi f_s t)$ were used to drive the outer PZT stacks. V_{dc} varied between -25 and 100 V, f_s varies between 20 and 90 Hz, and an oscillation amplitude of $5 V_{\text{rms}}$ was used for all measurements. The inner stack was compressed ($V_{\text{inner}} < 0$) to keep the sample under tension and avoid buckling or delaminating these soft, layered samples. While we do not have a direct *in situ* monitor for sample buckling during the experiment, bending and even partial delamination of some samples was observed at the conclusion of measurements with compressive stresses.

In order to disentangle effects which rely on the temperature and strain history of the sample, data were collected

using two different protocols. The first was to slowly sweep temperature while more rapidly stepping V_{outer} up and down. On each step, the dc component was changed by ± 12.5 V. Unless otherwise noted, data presented in the figures only shows data taken for steps which were increasing in voltage.

The second protocol used was to sweep temperature up and down for a fixed value of V_{dc} . This is not equivalent to measurement at constant strain. While the strain was monotonic in V_{dc} at any given temperature, temperature dependence of the displacement per volt in the PZT actuators caused the actual strain to drift as a function of temperature, as shown in Fig. 2(e).

The displacement ΔL of the jaws was measured using the capacitive sensor built into the CS-100 cell along with a bridge circuit described in Appendix B. Thermal expansion mismatch between the sample and the mounting materials, as well as the finite stiffness of the epoxy and cell itself, both produce temperature-dependent offsets of stress. These effects are discussed at length in Appendix C. The arguments of this paper, however, rely only on relative changes of stress—not the absolute stress values.

Samples are cleaved and cut by hand with a scalpel into rectangular bars of 1.3 – 2.4 mm in length, 250 – 500 μm in width, and 25 – 130 μm in thickness.

The quantity measured by the ac elastoresistivity technique in principle consists of a real (in-phase) component which contains information about the strain derivative of the resistivity and an imaginary (in-quadrature) component which contains information about dynamical or hysteretic effects [42,43]. Throughout this paper we focus only on the real part of the elastoresistivity signal and neglect the small, but finite, imaginary component. Understanding the

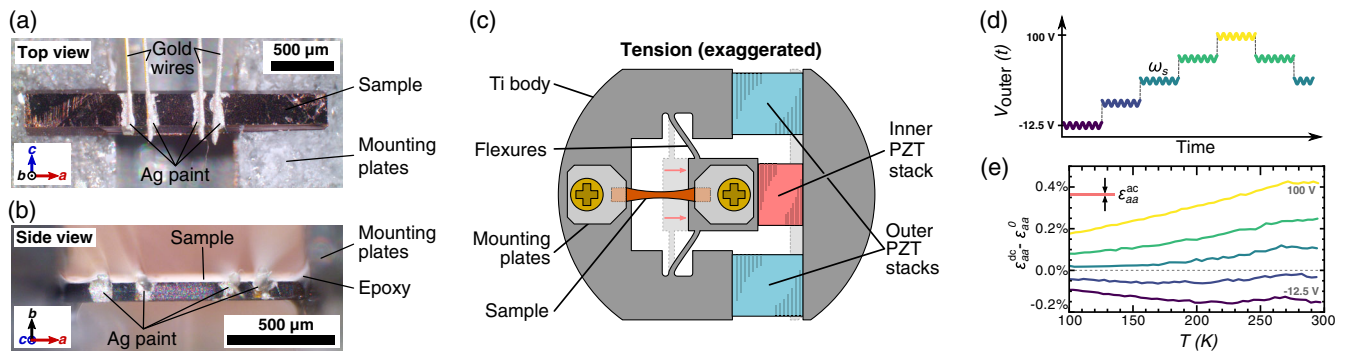


FIG. 2. Description of the experimental setup. (a) Microscope photograph of the top and (b) side of a representative ErTe_3 sample mounted in the stress cell, and contacted for a -axis resistivity and elastoresistivity measurements. (c) Illustration of the CS-100 stress cell from Razorbill Instruments. The outer two piezoelectric actuators were elongated ($V_{\text{outer}} > 0$) and the inner is compressed ($V_{\text{inner}} < 0$), resulting in tensile stress applied to the sample. (d) Schematic of the voltage applied to the outer stacks as a function of time. The actuator voltage was the sum of a stepwise dc offset (-25 to $+100$ V) with a small sinusoidal oscillation (ca. $5 V_{\text{rms}}$, 30 – 80 Hz). Data were taken continuously while the sample temperature was ramped slowly (approximately 1 K/min), and the duration of each dc step was approximately 6.5 s. (e) dc component of the strain measured for a representative ErTe_3 sample as a function of temperature and offset voltage V_{outer} . The temperature-dependent response of the piezoelectric actuators contributes to some drift in strain for any given temperature. The height of the shaded bar in the upper left-hand corner of (e) represents the maximum amplitude of the superimposed ac strain oscillation.

physical effects producing the quadrature signal would require a thorough investigation of the frequency dependence, which has not been conducted as part of this work.

IV. RESULTS

We now describe the various experimental results on $R\text{Te}_3$ under uniaxial stress, each of which provides further support of a strain-induced CDW realignment. We begin in Sec. IV A by probing the upper phase transition with the elastocaloric effect. Here, the reversal of a thermodynamic anomaly suggests a reversed anisotropy of the thermal expansion tensor, which we link to the CDW order parameter itself. Section IV B then describes the effect of uniaxial stress on all three components of the resistivity tensor. Here we show that while ρ_{bb} suggests the presence of a CDW gap regardless of stress, stress strongly suppresses gap-related effects in ρ_{aa} . Finally, Sec. IV D examines the elastoresistivity and confirms that the anti-symmetric, in-plane component of strain controls the strain-induced transition.

A. Thermodynamic evidence of CDW switching: Elastocaloric effect

The elastocaloric effect reflects the strain dependence of the entropy of a material. This can be detected experimentally through the change in temperature resulting from an adiabatic change in strain: $(dT/d\epsilon)_S$. Near phase transitions, ECE measurements manifest distinct anomalies, similar to those seen in heat capacity, due to strain dependence of the critical temperature [26]. More generally, though, the ECE is related to specific components of the elastic stiffness tensor, the thermal expansion tensor, and the heat capacity. Before discussing these relations in

greater detail, we first present the phenomenology uncovered by the ECE measurements of $R\text{Te}_3$.

The elastocaloric effect in ErTe_3 is presented in Fig. 3, and similar data for TmTe_3 are shown in Fig. 4. Figures 3(a) and 4(a) correspond to stress parallel to the a axis. For slightly compressive stresses (negative V_{outer}), a steplike anomaly at T_{CDW1} causes the ECE to increase in magnitude upon cooling through the transition (gray arrow marked “under compression”). Under these conditions, T_{CDW1} corresponds to the onset of the \mathbf{q}_c phase as in freestanding crystals. Increasing tensile strain causes the step first to shrink, then to invert such that the ECE decreases in magnitude upon cooling through T_{CDW1} (gray arrow marked “under tension”). At the largest tensile strains, the transition into the CDW state corresponds to an $\approx 85\%$ decrease of the total ECE signal.

We plot the strain dependence of T_{CDW1} in Fig. 3(b). We define ϵ_{aa}^0 as the strain for which T_{CDW1} reaches a minimum, corresponding to $\tilde{\epsilon}_A = 0$ in Sec. II. This point, where $dT_{\text{CDW1}}/d\epsilon$ changes sign, also corresponds to where the steplike anomaly flips its direction.

Such switching behavior is not observed for tensile stress parallel to the c axis, as seen for ErTe_3 in Fig. 3(c). In contrast to a -axis stress, even the most compressive traces correspond to a decrease in ECE magnitude upon cooling through T_{CDW1} . Additionally, increasing tensile strain slightly increases T_{CDW1} . For $T \lesssim 150$ K in both orientations, the ECE curves again become largely independent of both the orientation and magnitude of the stress.

ECE measurements in TmTe_3 for a -axis strain, shown in Fig. 4, follow the same trends as ErTe_3 . Cooling through T_{CDW1} (≈ 245 K) increases the ECE under compressive stress and decreases the ECE under tensile stress. T_{CDW1} also exhibits a weak minimum for small tensile stress.

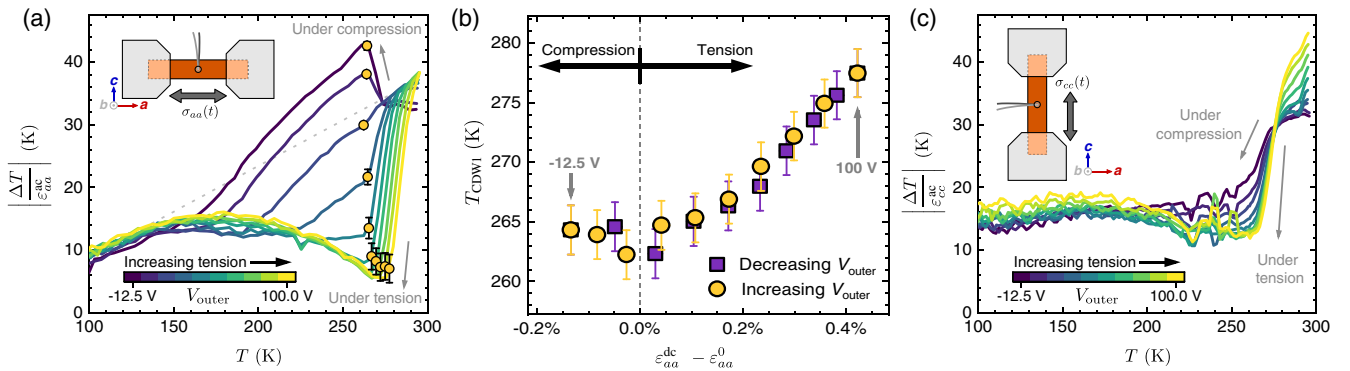


FIG. 3. Elastocaloric effect results for a sample of ErTe_3 with uniaxial stress (a) Magnitude of the elastocaloric response with stress parallel to the a axis as a function of temperature and offset voltage. The critical temperature T_{CDW1} (circles) is extracted from an extremum in the second derivative. Inset: schematic of the experimental setup. The dotted line is a guide to the eye for a linear background independent of strain. The anomaly at T_{CDW1} rises above this background for compressive stresses, but falls below this background for large enough tensile strain. (b) Critical temperatures T_{CDW1} extracted from (a) as a function of dc offset strain, shown for both increasing and decreasing PZT voltage steps. The critical temperature rises as one departs from ϵ_{aa}^0 toward either compressive or tensile strain. (c) Elastocaloric effect with stress parallel to the c axis. Tension increases the height of the critical anomaly, but no switching behavior is observed.

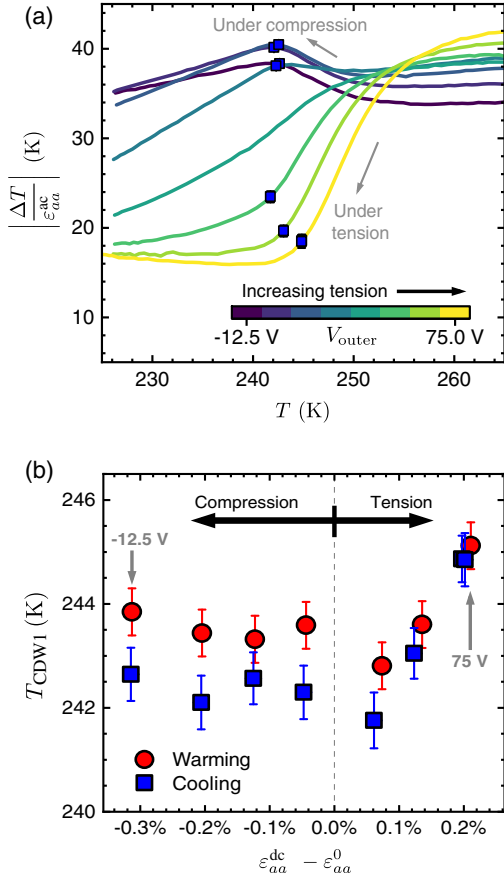


FIG. 4. Elastocaloric effect measurements in TmTe_3 with stress parallel to the a axis. (a) Magnitude of the elastocaloric response near T_{CDW1} as a function of temperature and PZT voltage. Each trace was collected by cooling at a constant V_{outer} , and T_{CDW1} is extracted by the second derivative. Despite using different data acquisition protocols and different rare earths, the results in Fig. 3 share the same behavior. (b) Extracted critical temperatures on the same sample for both warming and cooling traces. The increase of T_{CDW1} for tensile strains is clearly defined, although an increase on the compressive side is not observed. We attribute this to slight buckling of the sample, resulting in an overestimate of the compressive strain. One of the curves near the center exhibited no clear extremum in the second derivative, so T_{CDW1} could not be unequivocally identified. Tension and compression are labeled (black arrows) relative to $\tilde{\epsilon}_A = 0$.

We attribute the strain independence of T_{CDW1} on the compressive side to buckling of the sample. Buckling would imply poor transmission of strain into the sample, consistent with the smaller ECE signal observed for the most compressive case, $V_{\text{outer}} = -12.5$ V.

Each curve in Fig. 4 was taken on a separate temperature sweep with a constant voltage offset V_{dc} . The data in Fig. 3, in contrast, were all taken on the same temperature sweep, but stepping the voltage as in Fig. 2(d). Both, however, display the same qualitative features, indicating that this behavior is a robust feature of $R\text{Te}_3$ and does not depend on the stress and temperature history.

The change in behavior in the ECE between a -axis tension and compression can in principle arise from two separate physical effects. The first of these effects dominates at temperatures near a continuous phase transition, where the strength of the critical fluctuations depends on the reduced temperature $t = (T - T_c)/T_c$, where T_c is the critical temperature. If T_c is tuned adiabatically by an external parameter such as strain, the sample temperature will shift such that the total entropy is conserved. The smaller $|t|$, the larger the change in temperature. The resulting elastocaloric effect is proportional to the critical part of the specific heat $C_p^{(c)}$ and the rate of change of T_c with strain [26,44]:

$$\left(\frac{dT}{d\epsilon_{ij}}\right)_S = \frac{C_p^{(c)}}{C_p} \frac{dT_c}{d\epsilon_{ij}} + \dots \quad (7)$$

In $R\text{Te}_3$, we see that the change in sign of the ECE step occurs at the same strain as the change in sign of $dT_{\text{CDW1}}/d\epsilon$, consistent with this relation.

Heat capacity anomalies at T_{CDW1} have been observed to be quite small ($\approx 1\%$ of the total C_p) at both of the CDW transitions in TbTe_3 [45] and ErTe_3 [46]. The derivative of T_{CDW1} with respect to ϵ_{aa} is approximately 20 K/%. Using this value, Eq. (7) predicts an ECE anomaly at T_{CDW1} of approximately 20 K (0.2 K/%), which is indeed what is observed in both Figs. 3 and 4. In $R\text{Te}_3$, neither of the CDW transitions can be considered mean field [27,40,45], so some deviation from a mean-field step is expected.

This effect, however, only applies in the fluctuation regime within 10–20 K near T_{CDW1} [4]. Figure 3 shows that the sign-changing behavior of the ECE anomaly (subtracting a linear background) spans almost 100 K. Well below the transition, the strain-dependent ECE must therefore arise from a second effect, one due to the equilibrium CDW phase itself, rather than from critical fluctuations. A more general expression for the elastocaloric effect, valid at any temperature, relates the ECE to several thermodynamic properties,

$$\left(\frac{dT}{d\epsilon_{ij}}\right)_S = \frac{-T}{C_\sigma} C_{ijkl} \alpha_{kl}, \quad (8)$$

where C_σ is the specific heat at constant stress, C_{ijkl} is the elastic constant tensor, and α_{kl} is the thermal expansion tensor. Regardless of the strain in the sample, stability requires that C_σ and C_{ijkl} must retain the same sign, but α_{kl} has no such constraint. Therefore, a strain-induced change in the thermal expansion coefficients would explain the behavior of the ECE in $R\text{Te}_3$.

Previous x-ray measurements [30,47] indicate that the antisymmetric in-plane thermal expansion $\alpha_A = (\alpha_{cc} - \alpha_{aa})/2$ is negative below T_{CDW1} . Ordering of the \mathbf{q}_c CDW therefore reinforces the built-in orthorhombic distortion, increasing the c lattice parameter relative to a . The observed change in sign in the elastocaloric anomaly,

and therefore in the thermal expansion, suggests that the CDW wave vector has been switched from parallel to the c axis to parallel to the a axis.

B. Tracking changes in Fermi surface anisotropy: Resistivity

In this section, we describe measurements of all three components of the orthorhombic resistivity tensor as a function of temperature and applied stress. Electrical transport is highly sensitive to the opening of CDW gaps. These measurements show similar switching behavior as the ECE. Specifically, we show that a gap still opens in the strain-induced state, but at a different location on the Fermi surface, as would be expected from a CDW reorientation transition.

Previous results [35,48] have established that the onset of the first and second CDWs, with wave vectors directed along the c and a axis, respectively, invokes a larger change in ρ_{aa} and ρ_{cc} , respectively. This seemingly counterintuitive result arises due to the variation of the Fermi velocity around the Fermi surface, in conjunction with which sections of the FS are gapped at each CDW transition. In contrast, the longitudinal resistivity for currents running perpendicular to the Te planes ρ_{bb} is equally sensitive for both CDW transitions. Measurements of ρ_{bb} for ErTe₃ under a -axis stress are presented in Fig. 5. T_{CDW1} and T_{CDW2} are identified as minima in the temperature derivative.

We find that T_{CDW1} shows the same trend as ECE measurements—a weak minimum for small tensile stress. Combining the trend in T_{CDW1} with the ECE and resistivity measurements, we can conclude that the sample undergoes a phase transition which reorients the CDW wave vector and gap. Specifically, the height of the resistivity increase below T_{CDW1} , which is related to changes in the density of states at the Fermi level due to the opening of the CDW gap, decreases only slightly as stress increases. Because of the complex way in which the size, shape, and location of the CDW gap affect the electrical resistivity, the magnitude of the bump below T_{CDW1} should not be taken as a quantitative measure of the CDW gap. However, the persistence of a sharp peak in the derivative of ρ_{bb} suggests that a gap always opens somewhere on the quasi-2D FS. This suggests that the phase transition observed in ECE and in the trend of T_{CDW1} is a reorientation of the CDW wave vector.

T_{CDW2} decreases significantly as tensile strain increases, dropping ≈ 20 K for strains of 0.1%. Simultaneously, the corresponding bump in resistivity decreases in magnitude as well. Unlike T_{CDW1} , T_{CDW2} decreases monotonically with increasing tensile strain. We attribute this to an underestimate of the true tensile strain arising from mismatched thermal expansion between sample and the stress cell. The monotonic decrease in T_{CDW2} suggests that the tensile stress is, at these temperatures, beyond that required to realign the primary wave vector by 90°. The effects of thermal expansion mismatch are discussed in detail in Appendix C. This effect is also clearly visible in Fig. 9(b).

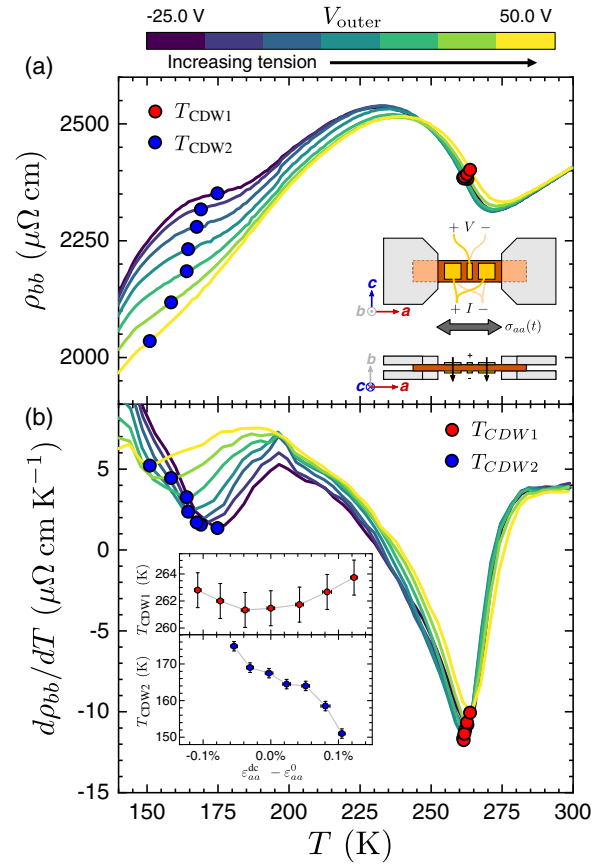


FIG. 5. Out-of-plane resistivity ρ_{bb} in ErTe₃. Panel (a) shows the resistivity traces for a series of PZT voltages. Inset: top and side view schematics of the contact geometry used in this experiment. Current is passed into the sample through the larger, outer two contacts on both the top and bottom of the crystal, and the smaller center pads are used to detect the voltage. Temperature derivatives of the resistivity traces are shown in (b). The minima of the derivative traces correspond to the critical temperatures. Inset of (b): T_{CDW1} and T_{CDW2} plotted as a function of strain. The lack of a maximum in T_{CDW2} corresponding to the minimum in T_{CDW1} and the switch between the two cases is attributed to an underestimate of the tensile stress arising from mismatched thermal expansion of the sample and stress cell.

The in-plane resistivity components, ρ_{aa} and ρ_{cc} , are presented in Fig. 6 for ErTe₃. These components show similar features at the CDW transitions, but also provide insight into the anisotropy of the Fermi surface in the ordered phases. As mentioned before, the CDW gap with wave vector \mathbf{q}_c has a larger effect on ρ_{aa} than on ρ_{cc} , and vice versa. This is observed clearly in Fig. 6(a) for a freestanding sample.

Figures 6(b) and 6(c) show measurements of both $\rho_{aa}(\epsilon)$ and $\rho_{cc}(\epsilon)$ with uniaxial stress parallel to the current flow. For slightly compressive a -axis stress, $\rho_{aa}(\epsilon)$ closely resembles the freestanding value, $\rho_{aa}(\epsilon = 0)$. As σ_{aa} increases, however, the change of ρ_{aa} across T_{CDW1} decreases in magnitude, and $\rho_{aa}(\epsilon_{aa})$ eventually behaves

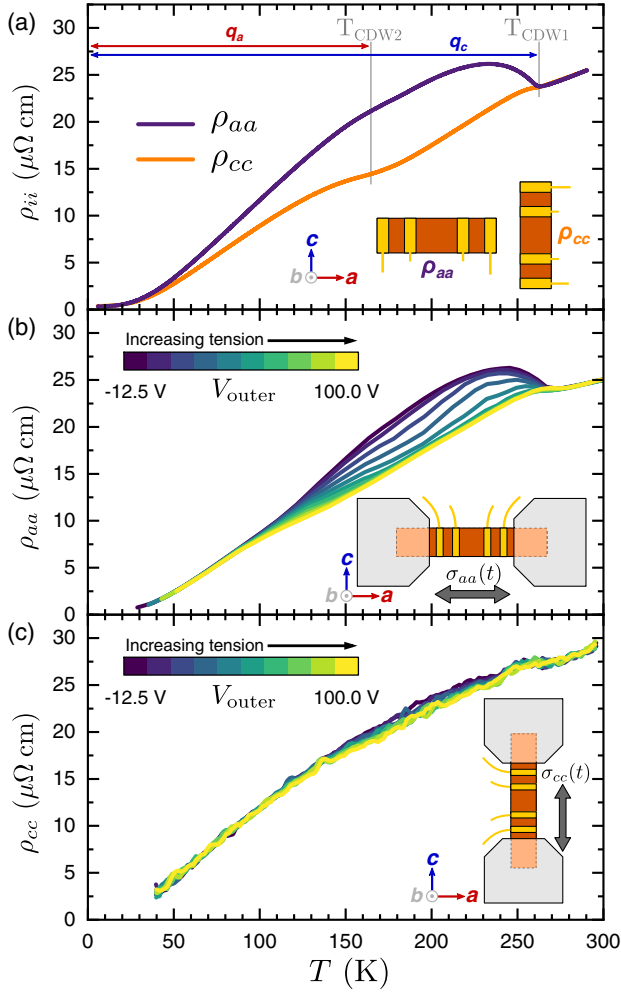


FIG. 6. In-plane resistivity components of ErTe₃ as a function of temperature and strain. (a) Freestanding resistivity components of ErTe₃. Resistivity along the a axis increases more strongly upon entering the \mathbf{q}_c state due to the curvature of the gapped region of the Fermi surface [35]. (b) a -axis resistivity of ErTe₃ under a -axis stress, as a function of temperature and PZT voltage. Negative and low voltages behave similarly to the freestanding case for ρ_{aa} , but crosses over to resemble freestanding ρ_{cc} as the tension increases. (c) c -axis resistivity under c -axis stress, which does not demonstrate any switching behavior.

like $\rho_{cc}(\varepsilon = 0)$ instead. In contrast, no such switching behavior is seen in $\rho_{cc}(\varepsilon)$. A slight decrease of the resistivity can be observed for the largest tensile stresses, but the curves never deviate very far from $\rho_{cc}(\varepsilon = 0)$.

Tensile σ_{cc} reinforces the intrinsic orthorhombicity of the material. Tensile σ_{aa} , however, opposes this orthorhombicity. In the simplified model presented in Sec. II, tensile σ_{aa} can train the CDW wave vector along \mathbf{q}_a . Our observation of clear switching behavior in ρ_{aa} , coupled with the persistence of a CDW gap in ρ_{bb} and a minimum in T_{CDW1} , supports this interpretation, and suggests a strain-tuned reorientation transition between \mathbf{q}_a and \mathbf{q}_c states. It is likely that compressive σ_{cc} would also cause a

reorientation, although sample buckling makes this regime inaccessible in the present experiment.

C. Evidence for first-order strain-induced transition: Hysteresis in resistivity

In order to examine the character of this putative reorientation transition, we have performed σ_{aa} stress cycles on a sample of ErTe₃ at constant temperature while measuring the a -axis resistivity, presented in Fig. 7. Above T_{CDW1} , very little strain-induced change in the resistivity is observed. As the sample cools below T_{CDW1} , a clear hysteresis loop opens. The exact size and shape of the hysteresis loops depends on the extent of the stresses applied, which depend on the history of the PZT actuators and is not identical between samples. The inset of Fig. 7 shows the normalized loop area for two different ErTe₃ samples in the same configuration. This hysteretic behavior below T_{CDW1} demonstrates that the switching behavior

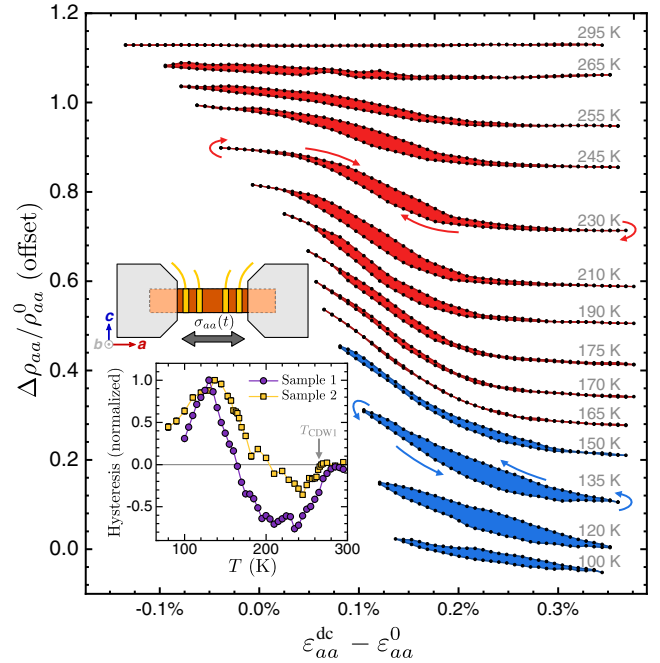


FIG. 7. Ratiometric change in ρ_{aa} of ErTe₃ through stress cycles performed at a few representative temperatures. Curves are offset vertically for clarity. Inset: schematic of the contact and stress geometry, and plot of the integrated area contained within the hysteresis loops in (b) for two different samples of ErTe₃. In both, the hysteresis loops open as the sample cools through T_{CDW1} . The hysteresis loop changes direction (clockwise to counterclockwise) as the temperature decreases further. The extracted area is sensitive to the exact dc strain range accessed, which accounts for the differences between samples. The observed hysteresis clearly indicates the first-order nature of the phase transition where the direction of the CDW wave vector switches from \mathbf{q}_a to \mathbf{q}_c , corresponding to the schematic phase diagram shown in Fig. 1(f).

seen in both the elastocaloric and resistivity data corresponds to a first-order transition.

Further decreases in temperature cause the hysteresis to close again, then reopen with the path oriented in the counterclockwise direction instead of clockwise. This inversion occurs near $T_{\text{CDW}2}$, although the exact value varies between the two samples. (Stress-cycle data for the second sample is shown in Appendix D.) Practical limitations in the stress cell (as described in Appendix C) caused the two measurements to cover slightly different ranges of strains—this in turn affects the details of the hysteresis loop shape and size. However, the presence of hysteresis, as well as the sign-changing behavior, appears to be robust.

The existence of a first-order transition and the vanishing hysteresis at a temperature below $T_{\text{CDW}1}$ are both consistent with the sixth-order free-energy expansion of Sec. II and Fig. 1(f). Equation (6) produces two multicritical points at the intersections between the first-order transition and $T_{\text{CDW}1}$ and $T_{\text{CDW}2}$. At either point, the transition between a \mathbf{q}_c and \mathbf{q}_a state must become continuous because the tunneling barrier will vanish.

The model of Eq. (6) does not, however, explain our observation of hysteresis for $T \lesssim T_{\text{CDW}2}$. At low temperatures, the model exhibits a single bidirectional CDW phase, free of any first-order transitions. Our measurements in Fig. 7 suggest, however, that a first-order transition does exist below $T_{\text{CDW}2}$. This low-temperature hysteresis may arise from subtle differences between the \mathbf{q}_a and \mathbf{q}_c phases; for instance, the magnitudes $|\mathbf{q}_c|$ and $|\mathbf{q}_a|$ differ slightly in freestanding samples [27,49]. This effect is neglected in Eq. (6), but details like this could introduce additional first-order transitions to the phase diagram. In any case, further experiments are required to fully explain these observations.

D. Disentangling in-plane symmetric and antisymmetric strains: Elastoresistivity

Finally, we turn to an elastoresistivity technique [42] to distinguish the effects of different strain components on the CDW state. The elastoresistivity tensor m_{ijkl} , which relates normalized changes in the resistivity tensor ρ_{ij} to the material strain ϵ_{kl} , is defined as

$$m_{ijkl} = \frac{d(\Delta\rho/\rho_0)_{ij}}{d\epsilon_{kl}}, \quad (9)$$

where $\delta\rho$ is the strain-induced change in resistivity and ρ_0 is the resistivity under zero strain conditions [50]. ER has proven a powerful tool in the understanding of symmetry-breaking phase transitions [52–55]. Figure 8 shows the in-plane, longitudinal ER responses of ErTe_3 under three different in-plane stress conditions.

Stress and current aligned with the a axis generates the largest ER as well as the largest stress dependence. We identify two persistent features in the data—the first, near $T_{\text{CDW}1}$, is a sharp dip toward negative ER values [red arrow in Fig. 8(a)]. Increasing tensile stress causes this feature to change sign, becoming a peak.

The second feature is a broad region (shaded in pink) of large negative ER. Increasing the tensile strain causes this “bulge” to increase in magnitude, then recede again. The largest magnitude (ER ≈ -225) is reached for the same stress at which the first feature changes sign.

In contrast, c -axis longitudinal ER [Fig. 8(c)] only shows behavior similar to the large stress limit of the a -axis ER. The same two features are present: a small peak near $T_{\text{CDW}1}$ (red arrow) and a broad minimum (shaded region) which shrinks with increasing tension.

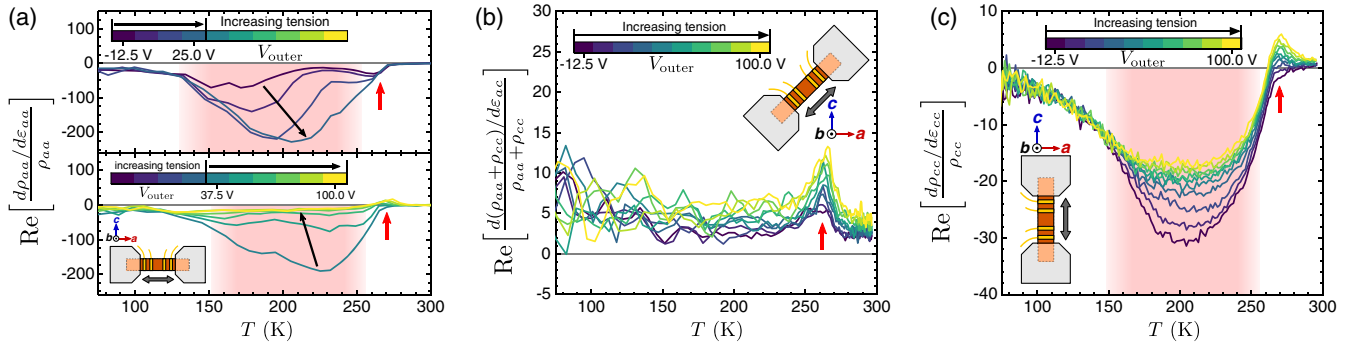


FIG. 8. (a)–(c) Longitudinal elastoresistivity components for ErTe_3 under three different stress orientations, as functions of temperature and PZT voltage. The results from the a -axis sample are split into two subpanels for clarity. Insets describe the orientation of the sample and current in each experiment. In the cases of a -axis and c -axis alignment, increasing tensile strain initially causes the growth of a large negative bulge (shaded in pink) between approximately 150 and 265 K, which then increases again for PZT voltages 37.5 V and above. The behavior in the bottom panel of (a) mimics that of (c), where tensile c -axis stress also decreases the magnitude of this negative bulge in the same temperature range. Diagonal stress, as shown in (b), does not generate any such response, indicating that the antisymmetric strain component $\epsilon_{aa} - \epsilon_{cc}$ dominates the changes in resistivity. A peak or dip localized at $T_{\text{CDW}1}$ (shown by the red arrow) appears in all three sample orientations although it carries the opposite sign for compressive and small tensile a -axis stress in the top panel of (a). This must therefore arise from the coupling of the CDW order parameter fluctuations to the in-plane symmetric strain or out-of-plane strain [26].

Finally, the longitudinal ER response aligned 45° to the orthorhombic axes [Fig. 8(b)] shows very different behavior. The small positive peak near T_{CDW1} is still present and increases in magnitude with tension. Below T_{CDW1} , however, the ER response is flat, small, and relatively insensitive to stress.

The orthorhombic symmetry group $Cmcm$ imposes very few constraints on the coupling between the CDWs and uniform strain ε_{ij} . Consider a generalized coupling of the form $\varepsilon_{ij}\Lambda_{ijk}|\psi_k|^2$, where $k = a, c$. Mirror planes impose $\Lambda_{ijk} = 0$ for $i \neq j$, but the six other terms remain free. In the tetragonal limit, one may take $\Lambda_{ijk} = \Lambda_{kji}$. However, as uniaxial stress experiments simultaneously tune several ε_{ij} components, disentangling the effects of each on the CDW is not trivial.

However, the three ER measurements presented in Fig. 8 allow us to identify the in-plane antisymmetric component of the strain, $\varepsilon_A = (\varepsilon_{aa} - \varepsilon_{cc})/2$, as the operative tuning parameter for the strain-induced transitions. Uniaxial stresses which do not generate a nonzero ε_A do not induce a transition. Furthermore, the in-plane symmetric component $\varepsilon_S = (\varepsilon_{aa} + \varepsilon_{cc})/2$ and the out-of-plane component ε_{bb} only contribute to shifts in critical temperature.

To see this, consider first the a - and c -axis elastoresistivity measurements. Both show similar phenomenology below T_{CDW1} under large tensile stress. Except for a small anisotropy in the elastic constants, these measurements are performed under similar magnitudes of ε_S , ε_{bb} , and ε_A , although the sign of ε_A will be flipped. Applying uniaxial stress along the in-plane diagonal results in $\varepsilon_A \approx 0$ and $\varepsilon_{ac} \neq 0$, although shear strain cannot couple (to linear order) to the CDW. The symmetric components ε_S and ε_{bb} will again be similar. This diagonal configuration effectively only probes the response to symmetric strains.

The large negative ER response present below T_{CDW1} in the a - and c -axis configurations can therefore only arise from coupling to ε_A . Meanwhile, the feature near T_{CDW1} , observed in all three measurements, must arise from coupling to symmetric strains ε_S and ε_{bb} . Near a strain-tuned continuous phase transition, ER will display similar singular behavior to the heat capacity [26]. We can therefore attribute this feature to changes in T_{CDW1} caused by ε_S and ε_{bb} .

Similar phenomenology is also seen for the a -axis ER in TmTe_3 [Fig. 9(a)]. A sharp feature (red arrow) is observed near T_{CDW1} , as well as a broad minimum in ER at lower temperatures. A critical value of stress ($V_{\text{outer}} \approx +12.5$) corresponds to both a change in sign of the peak at T_{CDW1} and the largest negative ER.

Additionally, a sharp local maximum is observed at low temperatures on the compressive side. On the tensile side, a similarly sharp minimum is observed—both of these features, given their opposing strain dependence, can be identified with T_{CDW2} and a transition into a bidirectional CDW state. With the exception of the most compressed

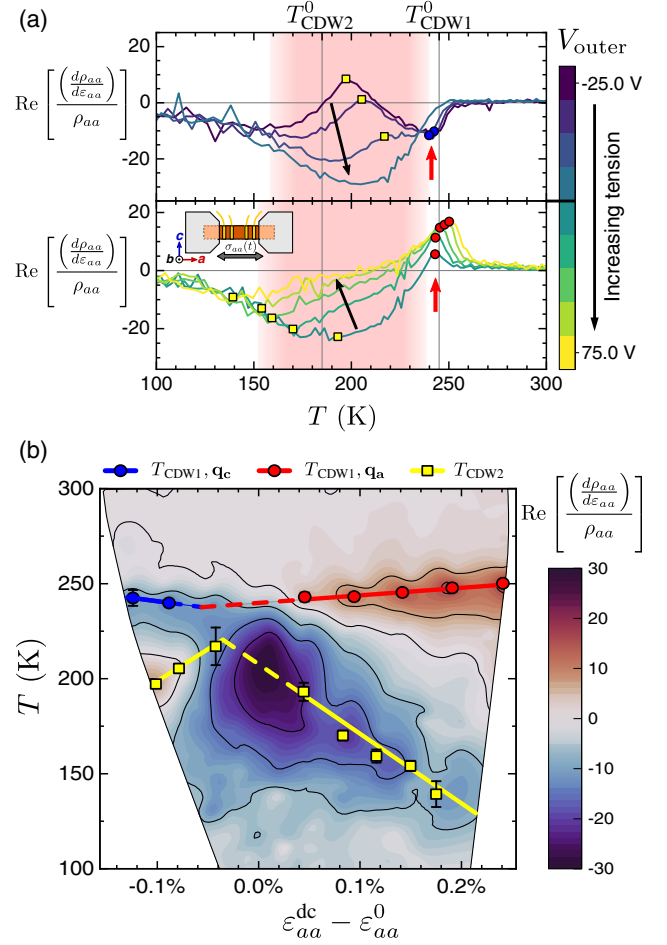


FIG. 9. Longitudinal a -axis elastoresistivity in TmTe_3 . Data presented here were taken by stepping the PZT voltage while sweeping temperature and extracted for steps of increasing tension only. (a) Elastoresistivity as a function of temperature and PZT voltage. Traces are all from the same sample, but have been separated into two panels for clarity. The top panel contains the responses for the most compressive, least tensile stress conditions, and the bottom for the largest tensile stresses. Short red arrows point out the peaks and dips attributed to T_{CDW1} , and the shaded regions highlight the “bulge” feature. (b) The same data as in (a) presented in the strain-temperature plane. Symbols correspond to the extracted extrema in the traces in (a). Solid lines are linear fits to the extracted transition positions and dotted lines denote an extrapolation to the intersection points. In conjunction with the evidence for a first-order transition as shown in Fig. 7, this diagram maps most closely onto the phase diagram presented in Fig. 1(f).

stress values, T_{CDW2} shows a similar monotonic decrease with stress, Fig. 5(b).

Figure 9(b) compiles the strain- and temperature-dependent evolution of the ER in TmTe_3 , as well as the extracted transition temperatures. Lines of best fit to T_{CDW1} and T_{CDW2} —the intersections of which highlight the likely positions of two separate multicritical points—highlight the fact that the phase diagram displays the same topology as

TABLE I. Rate of change of the critical temperatures T_{CDW1} and T_{CDW2} with strain in the strain-induced \mathbf{q}_a state. In all of these experiments, uniaxial stress is applied along the a axis. Not all techniques are sensitive to T_{CDW2} . The strain range of the ρ_{bb} measurements was insufficient to observe consistent linear behavior in T_{CDW1} . Sources of sample-to-sample variation are described in the text.

		$[(dT_{\text{CDW1}})/(d\epsilon_{aa})]$ (K/%)	$[(dT_{\text{CDW2}})/(d\epsilon_{aa})]$ (K/%)
ErTe ₃	ECE	47 ± 11	...
	ρ_{aa}	68.4 ± 6.7	...
	ρ_{bb}	...	-130 ± 16
TmTe ₃	ECE	22.1 ± 5.8	...
	ρ_{aa}	51.5 ± 6.7	...
	ER	43.7 ± 9.8	-221 ± 39

that produced in Fig. 1(f) by the free-energy expansion. Combined with the evidence for a first-order transition, the resulting phase diagram appears consistent with Fig. 1(f).

The change in critical temperatures for the strain-induced \mathbf{q}_a state under strain is presented in Table I. In general, T_{CDW2} is seen to be approximately 3–5 times more sensitive to strain than T_{CDW1} . The relatively large scatter in the different measurement techniques likely arises from uncertainty in the strain transmission from the stress cell to the sample, as well as run-to-run variations tentatively attributed to differences in the thickness of the epoxy layer used for mounting and uncertainties in the spacing between the mounting plates. Additionally, near the critical point the predicted sharp cusp in T_{CDW1} is seen to be rounded somewhat, likely due to strain inhomogeneities in the sample. This curvature can also lead to an underestimate of $dT_{\text{CDW1}}/d\epsilon_{aa}$. However, using a Young’s modulus E of approximately 50 GPa [56], these values agree with the range of values of $dT_{\text{CDW1}}/d\sigma_{aa} = E^{-1}(dT_{\text{CDW1}}/d\epsilon_{aa})$ previously reported for several $R\text{Te}_3$ compounds [45,46,57].

V. DISCUSSION

A phase transition induced by in-plane, antisymmetric strain in a weakly orthorhombic material raises a natural question of the existence of twin domains, either naturally occurring or induced by the applied stress. In the case of $R\text{Te}_3$, the most prevalent naturally occurring defect is a planar stacking fault normal to the b axis, at which the a and c axes swap directions. The existence of one or more of such stacking faults would tend to average the a - and c -axis observables together; we take the strikingly different behavior for stress along the a and c axes [Figs. 3(a) and 3(c) or Figs. 6(b) and 6(c), for example] as evidence that such stacking faults and misaligned domains are either not present or are sufficiently rare as to have negligible effect. Furthermore, macroscopic strains can neither couple to nor switch the direction of the glide plane itself due to the

nonsymmorphic nature of the crystal structure. In order to swap the symmetries of the a and c planes, one would need to shift every other $R\text{Te}$ block layer by $(a/2, 0, c/2)$. In-plane antisymmetric strain can only alter the dimensions of the unit cell, and the existence of any microscopic orthorhombic domains must rely only on the direction of the CDW ordering vector, not the crystal structure.

This work immediately suggests the application of other standard techniques to $R\text{Te}_3$ under uniaxial stress. X-ray diffraction, angle-resolved photoemission spectroscopy (ARPES), and pump-probe reflectivity or diffraction measurements under stress would be of particular interest. Diffraction measurements would enable the direct measurement of the intensity, position, and correlation length of the superlattice peaks at \mathbf{q}_a and \mathbf{q}_c simultaneously with the lattice strain. ARPES would provide direct verification and quantification of the CDW gap at \mathbf{q}_a . Other information could be gained through various ultrafast pump-probe techniques under strain as well; recent work has demonstrated that laser pulses on freestanding LaTe_3 can induce both topological defects in the CDW phase [58,59] and transient \mathbf{q}_a CDW correlations. These tools would provide a deeper understanding of the dynamics of the strain-induced \mathbf{q}_a state.

On a broader scale, $R\text{Te}_3$ offers a platform for systematic studies of the effects of chemical disorder on CDW-strain interactions. Several recent works [60–62] have shown that Pd atoms inserted between the Te bilayers (Pd_xRTe_3) act as a weak disorder potential which frustrates and suppresses long-range CDW order. Examination of the CDW correlations in Pd_xRTe_3 with scanning tunneling microscopy [41] suggests that increasing disorder may cause a cascade of “melting” transitions; the long-range-ordered CDW gives way first to a Bragg glass [63], then a vestigial nematic phase [17,19], before finally losing all long-range coherence for sufficiently strong disorder. Both of these intermediate phases break rotational symmetry and should therefore couple to in-plane antisymmetric strain. Uniaxial stress experiments such as those presented in this work, but applied to Pd_xRTe_3 , would enable both the substantiation of this phase diagram as well as an in-depth study of the properties of these phases and associate phase transitions. $R\text{Te}_3$ and Pd_xRTe_3 may be one of the few material systems in which the physics of these states can be examined systematically.

Expanding our focus beyond the $R\text{Te}_3$ family itself, understanding gained in experiments of strain- and disorder-tuned $R\text{Te}_3$ would also be particularly relevant for the case of the high- T_c cuprates, where disorder is an unavoidable side effect of chemical doping. Short- and long-range charge-ordered phases only appear in the cuprates at finite doping levels, but $R\text{Te}_3$, as a model system, may provide experimental access to an otherwise inaccessible limit of charge order on a square lattice in the absence of disorder. Having a chemically “clean” model system such as $R\text{Te}_3$

allows the experimenter to continuously track the evolution of symmetry-breaking effects (such as CDW correlations) and their sensitivity to in-plane antisymmetric strain as disorder is increased. In this way it may be possible to identify observed effects in disordered systems as the smeared, frustrated vestiges of phase transitions in the clean limit.

VI. CONCLUSIONS

In this work, we have shown that $R\text{Te}_3$, specifically ErTe_3 and TmTe_3 , provide a practical model system for the study of strain-CDW interactions. In particular, uniaxial stress can tune $R\text{Te}_3$ to and beyond a quasitragonal state for which the CDW wave vector realigns along the a axis rather than the c axis. We have shown that this phase transition occurs at uniaxial stress levels which are easily accessible in the laboratory. Through thermodynamic and transport measurements, we have established a phase diagram and identified several phase transitions: a second-order transition to the \mathbf{q}_a -only state upon cooling under uniaxial stress, and a first-order transition between the \mathbf{q}_c and \mathbf{q}_a states induced by uniaxial stress for temperatures below $T_{\text{CDW}1}$. The observed phenomena map directly to a sixth-order free-energy expansion. This work motivates the application of x-ray scattering and ARPES studies of $R\text{Te}_3$ under strain to further quantify the behavior and characteristics of the strain-induced \mathbf{q}_a state. Extension of the techniques presented here to samples with quenched disorder, such as Pd_xRTe_3 , may also provide unique insight into forms of frustrated charge order on a tetragonal lattice under uniaxial stress.

ACKNOWLEDGMENTS

The authors wish to thank Steve Kivelson for insightful discussions. This work was supported by the U.S. Department of Energy, Office of Basic Sciences, under Contract No. DE-AC02-76SF00515. Part of this work was performed at the Stanford Nano Shared Facilities (SNSF)/Stanford Nanofabrication Facility (SNF), supported by the National Science Foundation under Grant No. ECCS-1542152.

APPENDIX A: DETAILS OF SAMPLE PREPARATION

The in-plane a and c axes of samples are distinguished using x-ray diffraction by comparing amplitudes of the (061) peak with its forbidden counterpart (160). Samples were epoxied and clamped to the stress cell between a set of roughened titanium mounting plates. The sample is electrically isolated from the bottom titanium mounting plates with small pieces of thin tissue paper impregnated with epoxy. The distance between the edges of the clamps is approximately 1 mm.

We include the effect of thermal contraction of the plates of the capacitive sensor itself, and at any given temperature we use the measured plate spacing as the sample length L .

This protocol, while complicated, minimizes the time allowed for thermal and mechanical drifts in the apparatus. The voltage-strain relationship of the PZT stacks depends strongly on temperature and voltage history, and a smooth slow temperature ramp, rather than a series of temperature steps and the associated equilibration time at each step, produces the widest, highest resolution coverage of the stress-temperature space in the shortest time. The cases of increasing and decreasing voltages differ by a slight hysteresis ascribed to the presence of a first-order transition (to be discussed in detail below) but otherwise show the same qualitative behavior. Figure 7 shows a direct comparison of data taken on increasing and decreasing voltage steps, and Fig. 3(b) shows critical temperatures extracted from both increasing and decreasing voltage steps.

Electrical contacts are formed by sputtering gold onto the freshly cleaved surface, and gold wires are attached with DuPont 4929 silver paint. All of the contacts are placed within the suspended section of the crystal to minimize contributions from the clamped regions, which may experience significant strain inhomogeneity. The resistivity and elastoresistivity are extracted simultaneously using the demodulation techniques presented in Ref. [42]. The voltage signal is amplified through an SR554 transformer from Stanford Research Systems with gain of 100. The transformer's frequency dependence is independently calibrated and measured signals are corrected to reflect this.

We detect strain-induced oscillations in the sample temperature using a thermocouple. A type E thermocouple [64] is formed by spot welding pieces of constantan and chromel thermocouple wire, both 12.5 μm in diameter. The welded junction is then attached to the center of the top face of the sample using either two-part epoxy or silver paint. The reference junction is formed by attaching the free ends of the wires to copper pads which are thermalized to the body of the strain cell, as in Ref. [44]. The detected signal is amplified with an SR554 transformer as well as an SR560 preamplifier, together providing a composite gain of 2000.

APPENDIX B: ac CAPACITANCE MEASUREMENTS

The CS-100 uniaxial strain cell from Razorbill Instruments incorporates a capacitive displacement sensor used to quantify the strain in the sample. Highly accurate measurements of the capacitance can be made for quasi-static cell displacements, but techniques for measuring changes in capacitance occurring at frequencies above a few hertz are not well established. To make it possible to accurately quantify the oscillating strains, and therefore the magnitudes of the elastoresistivity and elastocaloric effect, we have developed a custom bridge circuit (based on a commonly used impedance measurement technique)

which, in conjunction with a pair of lock-in amplifiers, measures both dc and ac changes in capacitance. The bridge is based on an autobalancing bridge topology, which can effectively cancel effects of parasitic capacitances due to the cables.

A simplified circuit schematic is shown in Fig. 10. An ac voltage (amplitude 0.5 V, frequency around 20 kHz) is applied to the input terminal, passed through a unity-gain buffer Q_1 to minimize the output impedance, and then passed to the CS-100 displacement sensor through a coaxial cable. The capacitance of the sensor is of order 1 pF and varies approximately ± 250 fF through the full range of displacements. In comparison, typical capacitances for the coaxial cables required to connect the circuit (at room temperature) to the stress cell inside the cryostat are of order 100 pF, more than 2 orders of magnitude larger than the changes to be observed. The low output impedance of the first buffer stage prevents phase lag due to charging and discharging of this parasitic cable capacitance C_{p1} .

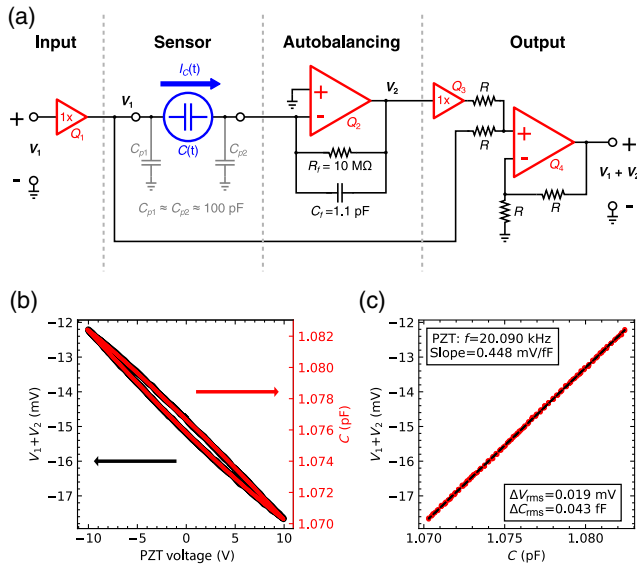


FIG. 10. Construction and calibration of the autobalancing capacitance bridge. (a) Diagram of the circuit employed here. An ≈ 20 kHz reference input sine wave (V_1) is buffered at the input, then applied to one terminal of the displacement sensor through coaxial cables. The opposite terminal is connected to a virtual ground by the autobalancing section, where the feedback capacitor acts as a reference. The output V_2 of the autobalancing bridge will be a sine wave with magnitude proportional to the ratio of the sensor and reference capacitances, but 180° out of phase with the reference. The signals at V_1 and V_2 are added together with a noninverting summing amplifier, and the two will cancel if the sensor and reference capacitances are equal. (b) Output of the capacitance bridge (right-hand axis) overlaid with independent quasistatic measurements made with a commercial capacitance bridge. (c) The output voltage plotted against the measured capacitance, demonstrating linear behavior and a sensitivity of $448 \mu\text{V}/\text{fF}$ and a root-mean-square noise floor of 43 aF. This corresponds to a displacement of approximately 2 nm.

The other terminal of the capacitive sensor is connected to a virtual ground at the inverting terminal of the autobalancing stage. The feedback network of this stage contains a capacitor which acts as the reference, as well as a resistor for stability. The output of this stage is such that the second terminal of the capacitive sensor remains at 0 V, implying that the parasitic capacitance C_{p2} at this terminal does not draw any current. The output voltage V_2 required for this is proportional to the ratio of the sensor capacitance $C(t)$ to the reference capacitance C_f , but with opposite sign. The final stage combines the output V_2 with the input reference signal such that the two cancel exactly when $C(t) = C_f$.

The magnitude of the sum is detected by a lock-in amplifier. Knowing C_f , the time-averaged magnitude can then be converted to provide a measurement of the dc capacitance. The instantaneous magnitude as it appears at the output of the lock-in amplifier, however, still contains the modulation at the strain frequency; a second demodulation stage of this signal provides direct access to the magnitude of the ac capacitance variation.

We have calibrated our bridge circuit against a commercial capacitance bridge for quasistatic strain, as shown in Figs. 10(b) and 10(c), and found that the behavior is well within the linear regime. The capacitance-to-voltage conversion factor is approximately $0.448 \text{ mV}/\text{fF}$, and the noise floor is approximately 43 aF. By simulating the strain-modulated capacitance sensor with an amplitude-modulated current source, we have also confirmed that the circuit described here maintains its accuracy to within 2% for strain frequencies up to 1 kHz. Typical changes in capacitance for a 5 V_{rms} oscillating voltage on the outer pair of piezoelectric stacks range between 0.75 fF at 20 K to approximately $2.5 \text{ fF}_{\text{rms}}$ at room temperature.

APPENDIX C: EFFECTS OF THERMAL EXPANSION MISMATCH, FINITE EPOXY STIFFNESS

In an ideal case, where the stress cell and epoxy would be infinitely stiff compared to the sample, the sample strain is given by $\varepsilon = \Delta L/L$, where L is the sample length and ΔL is the displacement detected by the capacitive sensor. This case would be equivalent to the thermodynamic condition of fixing constant strain along the long axis of the sample (temporarily defining this as the x -axis ε_{xx}) while the other components of the strain tensor are allowed to relax. This differs slightly from the conditions described in the guiding model of the previous section, in which $\bar{\sigma}_{xx}$ was held constant. In a freestanding crystal, the coupling terms between the CDW and strain [λ and η in Eq. (5)] cause strain to behave like a secondary order parameter. A finite value of the CDW gap in either direction induces a sympathetic orthorhombic distortion. Fixing constant strain rather than stress would largely preserve the phase diagram

of Fig. 1(f) except near the \mathbf{q}_a - \mathbf{q}_c transition—the first-order transition would widen to encompass a region characterized by a patchwork of orthogonal domains of $|\tilde{\epsilon}_A| > 0$ such that the average strain matched the externally imposed condition. In reality, however, we must mention three caveats regarding this idealized constant-strain condition.

First, the pliability of the epoxy is known to decrease the strain transmitted to the sample. Simulations for the case of iron-pnictide superconductor samples show strain transmission of approximately 70% the ideal value [65]. This effect changes quantitative estimates of critical values of the strain to induce the phase transition shown in Fig. 1(f), but does not affect the overall features of the phase diagram. For the present study we therefore neglect this effect since our focus is on general features of the strain-tuned phase diagram.

Second, mismatch of the thermal expansion coefficients between the sample and titanium cell body generates a temperature-dependent stress. In the case of $R\text{Te}_3$, the in-plane thermal expansion is approximately 5 times larger than that of titanium at room temperature [30]. While the thermal expansion of $R\text{Te}_3$ has not been measured for all temperatures, it is sensible to assume that the estimated magnitude of tensile (compressive) strain is always underestimated (overestimated). In the absence of a direct measure of the $R\text{Te}_3$ lattice parameter, we have chosen not to apply any offset corrections to the reported strains throughout this work. Doing so would require extrapolations from diffraction measurements on freestanding samples, but such extrapolations would not apply to a state in which the CDW has been rotated by strain. The cost of neglecting the sample thermal expansion in this calculation is a negligible underestimate of the magnitude of the strain oscillations, and the inclusion of an unknown and temperature-dependent strain offset.

Finally, the process of curing the mounting epoxy can produce built-in strains even at room temperature, and this offset varies from sample to sample. In order to compare samples on the same scale, we extract the location of the critical point between the \mathbf{q}_c , \mathbf{q}_a , and disordered states, which we define as occurring at the degeneracy strain ϵ_{aa}^0 . The arguments provided in this paper do not require the exact knowledge of the absolute strain, but rather focus on the relative changes.

APPENDIX D: HYSTERESIS MEASUREMENTS IN SECOND SAMPLE

Figure 11 shows the stress-cycle data for the a -axis resistivity of a second ErTe_3 sample, similar to Fig. 7. As seen in the previous sample, hysteresis becomes apparent below $T_{\text{CDW}1}$, then changes directions on further decreases of temperature. In this sample, due to subtle differences in experimental details (see Appendix C) the accessible range of strain does not appear to include the lower coercive strain; the resistivity is not seen to saturate on the

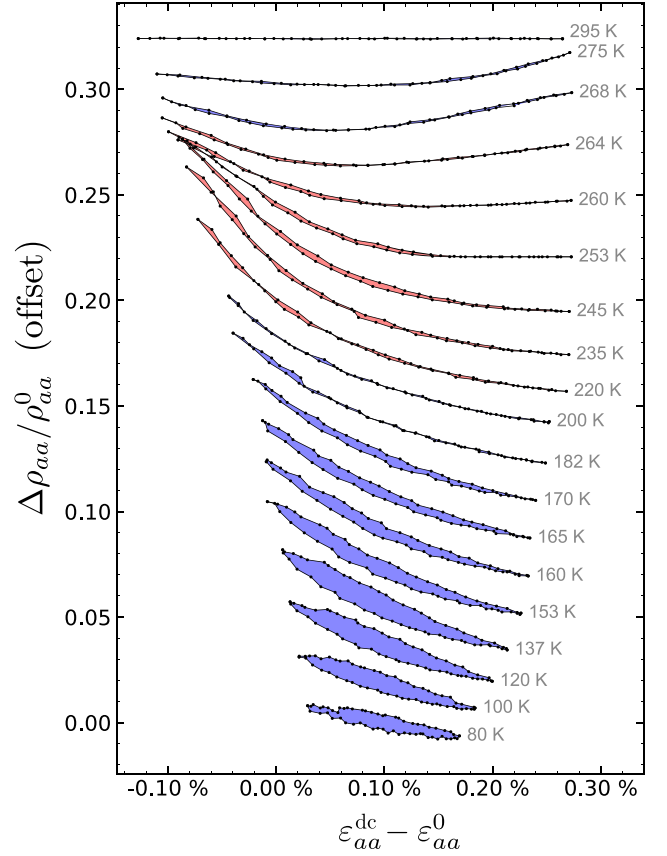


FIG. 11. Resistivity stress-cycle data for a second sample of ErTe_3 , showing a similar phenomenon, but with a decreased magnitude of the effect. We attribute this difference to differences in the accessible range of strains in our experimental setup.

compressive side as in Fig. 7. As a result, the magnitude of the hysteresis is substantially decreased. The qualitative structure, however, appears largely the same.

APPENDIX E: FREQUENCY DEPENDENCE OF ECE MEASUREMENTS

As described in detail in Ref. [44], the criteria for quasiadiabatic behavior in ECE measurements depend on the thermal properties of the sample, as well as the properties of the materials used to mount the sample and to adhere the thermocouple. At low strain frequencies, the sample tends to thermalize with the mounting plates, decreasing the observed temperature oscillation magnitude. At high strain frequencies, the thermocouple can no longer follow the changes in temperature. The maximum signal is observed at intermediate frequencies. Formally, the low frequency cutoff for quasiadiabatic behavior ω_{qa} depends on the thermal conductivity κ , the volumetric specific heat ρc_p , and the sample length L as

$$\omega_{qa} \propto \frac{\kappa}{\rho c_p L^2}. \quad (\text{E1})$$

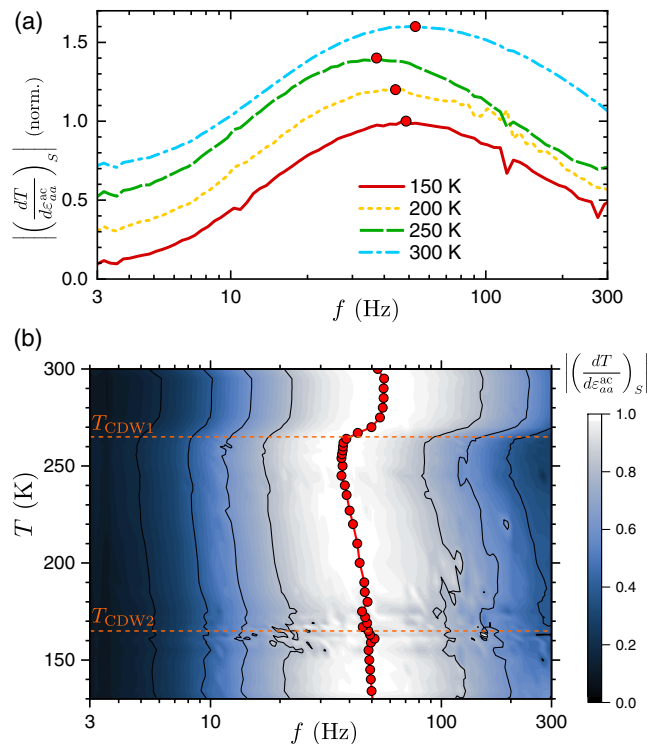


FIG. 12. Frequency dependence of elastocaloric effect measurements on ErTe_3 under a -axis stress. (a) Magnitude of the ECE signal as a function of strain frequency for several representative temperatures. Each curve is normalized to the maximum signal observed at that temperature, and the curves are vertically offset for clarity. The peak is notated with a red circle. Panel (b) shows similar data for a dense set of temperatures, presented as a contour plot. As the sample cools below T_{CDW1} , the peak frequency decreases from approximately 55 Hz to approximately 35 Hz. This shift in the peak frequency reflects a sudden decrease in thermal conductivity. This is qualitatively consistent with the Wiedemann-Franz law: this measurement is most sensitive to the thermal conductivity along the a axis, and the electrical resistivity ρ_{aa} also shows the highest increase when cooling through T_{CDW1} . Data presented in the main text were acquired for a constant frequency in the range of 20–40 Hz. Shifts in the frequency dependence with temperature will affect the absolute magnitudes of the ECE signals in Figs. 3 and 4, but would alter neither qualitative behavior nor the conclusions stemming from this data.

As a consequence, any changes in the thermal conductivity or specific heat will result in a change of the observed elastocaloric signal.

Upon cooling, as one passes through the CDW transition temperature T_{CDW1} , the electrical resistivity is shown in Fig. 6 to change significantly, especially ρ_{aa} . The Wiedemann-Franz law suggests that a similar change would be observed in the thermal conductivity. The temperature-dependence data presented in Figs. 3 and 4 were taken using a single frequency for the entire temperature and strain range; the temperature dependence of the thermal conductivity should be expected to alter the signal.

Figure 12 shows the frequency dependence of magnitude of the elastocaloric effect for a -axis stress on ErTe_3 as a function of temperature. The frequency f_p at which the ECE reaches its peak is denoted by the filled symbols. As the sample is cooled through T_{CDW1} , the location of the maximum moves to lower frequencies, corresponding to a change in the ratio κ/c_p . The heat capacity, which is dominated by the phonon background (the Debye temperature $\Theta_D \approx 180$ K [27,34]), is known to be approximately constant through T_{CDW1} [46]. Therefore, the change in the frequency dependence must arise from changes in the thermal conductivity.

Two different contributions to the ECE anomaly at T_{CDW1} were discussed in the main text: critical fluctuations near a strain-tuned phase transition and changes in the thermal expansion tensor. For an ECE measurement at a constant frequency f_0 , however, a sharp change in the frequency dependence can also contribute to this anomaly. If $f_0 < f_p$, the frequency dependence would cause the ECE magnitude to rise upon cooling through T_{CDW1} . The ECE measurements in Figs. 3 and 4 were made with strain frequencies of 37 and 51 Hz, respectively. The ECE anomaly in the near-freestanding case does indeed increase the ECE magnitude on cooling through T_{CDW1} , implying that a frequency dependence could indeed be contributing to the behavior. However, both the \mathbf{q}_c and strain-induced \mathbf{q}_a states should correspond to a decrease in thermal conductivity due to the opening of a CDW gap. Therefore we conclude that changes in the frequency dependence can decrease the size of the ECE anomaly, but such changes cannot explain the change in sign of the anomaly. Frequency-dependent effects can at most alter the absolute magnitude, but the effects discussed in the main text must still be the primary contributions to the ECE.

- [1] E. DiMasi, M. C. Aronson, J. F. Mansfield, B. Foran, and S. Lee, *Chemical Pressure and Charge-Density Waves in Rare-Earth Tritellurides*, *Phys. Rev. B* **52**, 14516 (1995).
- [2] G.-H. Gweon, J. D. Denlinger, J. A. Clack, J. W. Allen, C. G. Olson, E. D. DiMasi, M. C. Aronson, B. Foran, and S. Lee, *Direct Observation of Complete Fermi Surface, Imperfect Nesting, and Gap Anisotropy in the High-Temperature Incommensurate Charge-Density-Wave Compound SmTe_3* , *Phys. Rev. Lett.* **81**, 886 (1998).
- [3] M. D. Johannes and I. I. Mazin, *Fermi Surface Nesting and the Origin of Charge Density Waves in Metals*, *Phys. Rev. B* **77**, 165135 (2008).
- [4] H.-M. Eiter, M. Lavagnini, R. Hackl, E. A. Nowadnick, A. F. Kemper, T. P. Devereaux, J.-H. Chu, J. G. Analytis, I. R. Fisher, and L. Degiorgi, *Alternative Route to Charge Density Wave Formation in Multiband Systems*, *Proc. Natl. Acad. Sci. U.S.A.* **110**, 64 (2013).
- [5] M. Maschek, D. A. Zocco, S. Rosenkranz, R. Heid, A. H. Said, A. Alatas, P. Walmsley, I. R. Fisher, and F. Weber,

- Competing Soft Phonon Modes at the Charge-Density-Wave Transitions in DyTe₃*, *Phys. Rev. B* **98**, 094304 (2018).
- [6] R. E. Peierls, *Quantum Theory of Solids* (Oxford University Press, New York, 2001).
- [7] S. K. Chan and V. Heine, *Spin Density Wave and Soft Phonon Mode from Nesting Fermi Surfaces*, *J. Phys. F* **3**, 795 (1973).
- [8] H. Requardt, J. E. Lorenzo, P. Monceau, R. Currat, and M. Krisch, *Dynamics in the Charge-Density-Wave System NbSe₃ Using Inelastic X-Ray Scattering with meV Energy Resolution*, *Phys. Rev. B* **66**, 214303 (2002).
- [9] M. Leroux, I. Errea, M. Le Tacon, S.-M. Souliou, G. Garbarino, L. Cario, A. Bosak, F. Mauri, M. Calandra, and P. Rodière, *Strong Anharmonicity Induces Quantum Melting of Charge Density Wave in 2H-NbSe₂ under Pressure*, *Phys. Rev. B* **92**, 140303(R) (2015).
- [10] M. Maschek, S. Rosenkranz, R. Hott, R. Heid, M. Merz, D. A. Zocco, A. H. Said, A. Alatas, G. Karapetrov, S. Zhu, J. van Wezel, and F. Weber, *Superconductivity and Hybrid Soft Modes in TiSe₂*, *Phys. Rev. B* **94**, 214507 (2016).
- [11] J. J. Hamlin, D. A. Zocco, T. A. Sayles, M. B. Maple, J. H. Chu, and I. R. Fisher, *Pressure-Induced Superconducting Phase in the Charge-Density-Wave Compound Terbium Tritelluride*, *Phys. Rev. Lett.* **102**, 177002 (2009).
- [12] A. Soumyanarayanan, M. M. Yee, Y. He, J. V. Wezel, D. J. Rahn, K. Rossnagel, E. W. Hudson, M. R. Norman, and J. E. Hoffman, *Quantum Phase Transition from Triangular to Stripe Charge Order in NbSe₂*, *Proc. Natl. Acad. Sci. U.S.A.* **110**, 1623 (2013).
- [13] F. Flicker and J. van Wezel, *Charge Ordering Geometries in Uniaxially Strained NbSe₂*, *Phys. Rev. B* **92**, 201103(R) (2015).
- [14] D. A. Zocco, J. J. Hamlin, K. Grube, J.-H. Chu, H.-H. Kuo, I. R. Fisher, and M. B. Maple, *Pressure Dependence of the Charge-Density-Wave and Superconducting States in GdTe₃, TbTe₃, and DyTe₃*, *Phys. Rev. B* **91**, 205114 (2015).
- [15] S. Lei, J. Lin, Y. Jia, M. Gray, A. Topp, G. Farahi, S. Klemenz, T. Gao, F. Rodolakis, J. L. McChesney, C. R. Ast, A. Yazdani, K. S. Burch, S. Wu, N. P. Ong, and L. M. Schoop, *High Mobility in a van der Waals Layered Antiferromagnetic Metal*, *Sci. Adv.* **6**, eaay6407 (2020).
- [16] B. Sharma, M. Singh, B. Ahmed, B. Yu, P. Walmsley, I. R. Fisher, and M. C. Boyer, *Interplay of Charge Density Wave States and Strain at the Surface CeTe₂*, *Phys. Rev. B* **101**, 245423 (2020).
- [17] L. Nie, G. Tarjus, and S. A. Kivelson, *Quenched Disorder and Vestigial Nematicity in the Pseudogap Regime of the Cuprates*, *Proc. Natl. Acad. Sci. U.S.A.* **111**, 7980 (2014).
- [18] R. M. Fernandes, S. A. Kivelson, and E. Berg, *Vestigial Chiral and Charge Orders from Bidirectional Spin-Density Waves: Application to the Iron-Based Superconductors*, *Phys. Rev. B* **93**, 014511 (2016).
- [19] L. Nie, A. V. Maharaj, E. Fradkin, and S. A. Kivelson, *Vestigial Nematicity from Spin and/or Charge Order in the Cuprates*, *Phys. Rev. B* **96**, 085142 (2017).
- [20] R. M. Fernandes, P. P. Orth, and J. Schmalian, *Intertwined Vestigial Order in Quantum Materials: Nematicity and Beyond*, *Annu. Rev. Condens. Matter Phys.* **10**, 133 (2019).
- [21] W. Tabis, Y. Li, M. L. Tacon, L. Braicovich, A. Kreyssig, M. Minola, G. Dellea, E. Weschke, M. J. Veit, M. Ramazanoglu, A. I. Goldman, T. Schmitt, G. Ghiringhelli, N. Barišić, M. K. Chan, C. J. Dorow, G. Yu, X. Zhao, B. Keimer, and M. Greven, *Charge Order and Its Connection with Fermi-Liquid Charge Transport in a Pristine High-T_c Cuprate*, *Nat. Commun.* **5**, 5875 (2014).
- [22] R. Comin, R. Sutarto, F. He, E. H. da Silva Neto, L. Chauviere, A. Frañó, R. Liang, W. N. Hardy, D. A. Bonn, Y. Yoshida, H. Eisaki, A. J. Achkar, D. G. Hawthorn, B. Keimer, G. A. Sawatzky, and A. Damascelli, *Symmetry of Charge Order in Cuprates*, *Nat. Mater.* **14**, 796 (2015).
- [23] S. Gerber *et al.*, *Three-Dimensional Charge Density Wave Order in YBa₂Cu₃O_{6.67} at High Magnetic Fields*, *Science* **350**, 949 (2015).
- [24] H. Jang *et al.*, *Ideal Charge-Density-Wave Order in the High-Field State of Superconducting YBCO*, *Proc. Natl. Acad. Sci. U.S.A.* **113**, 14645 (2016).
- [25] J.-J. Wen, H. Huang, S.-J. Lee, H. Jang, J. Knight, Y. S. Lee, M. Fujita, K. M. Suzuki, S. Asano, S. A. Kivelson, C.-C. Kao, and J.-S. Lee, *Observation of Two Types of Charge-Density-Wave Orders in Superconducting La_{2-x}Sr_xCuO₄*, *Nat. Commun.* **10**, 3269 (2019).
- [26] A. T. Hristov, M. S. Ikeda, J. C. Palmstrom, P. Walmsley, and I. R. Fisher, *Elastoresistive and Elastocaloric Anomalies at Magnetic and Electronic-Nematic Critical Points*, *Phys. Rev. B* **99**, 100101(R) (2019).
- [27] A. Banerjee, Y. Feng, D. M. Silevitch, J. Wang, J. C. Lang, H. H. Kuo, I. R. Fisher, and T. F. Rosenbaum, *Charge Transfer and Multiple Density Waves in the Rare Earth Tellurides*, *Phys. Rev. B* **87**, 155131 (2013).
- [28] W. L. McMillan, *Landau Theory of Charge-Density Waves in Transition-Metal Dichalcogenides*, *Phys. Rev. B* **12**, 1187 (1975).
- [29] C. D. Malliakas and M. G. Kanatzidis, *Divergence in the Behavior of the Charge Density Wave in RETe₃ (RE = Rare-Earth Element) with Temperature and RE Element*, *J. Am. Chem. Soc.* **128**, 12612 (2006).
- [30] N. Ru, C. L. Condon, G. Y. Margulis, K. Y. Shin, J. Laverock, S. B. Dugdale, M. F. Toney, and I. R. Fisher, *Effect of Chemical Pressure on the Charge Density Wave Transition in Rare-Earth Tritellurides RTe₃*, *Phys. Rev. B* **77**, 035114 (2008).
- [31] A. Fang, N. Ru, I. R. Fisher, and A. Kapitulnik, *STM Studies of TbTe₃: Evidence for a Fully Incommensurate Charge Density Wave*, *Phys. Rev. Lett.* **99**, 046401 (2007).
- [32] L. Fu, A. M. Kraft, B. Sharma, M. Singh, P. Walmsley, I. R. Fisher, and M. C. Boyer, *Multiple Charge Density Wave States at the Surface of TbTe₃*, *Phys. Rev. B* **94**, 205101 (2016).
- [33] U. Ralević, N. Lazarević, A. Baum, H.-M. Eiter, R. Hackl, P. Giraldo-Gallo, I. R. Fisher, C. Petrovic, R. Gajić, and Z. V. Popović, *Charge Density Wave Modulation and Gap Measurements in CeTe₃*, *Phys. Rev. B* **94**, 165132 (2016).
- [34] N. Ru and I. R. Fisher, *Thermodynamic and Transport Properties of YTe₃, LaTe₃, and CeTe₃*, *Phys. Rev. B* **73**, 033101 (2006).
- [35] A. A. Sinchenko, P. D. Grigoriev, P. Lejay, and P. Monceau, *Spontaneous Breaking of Isotropy Observed in the*

- Electronic Transport of Rare-Earth Tritellurides*, *Phys. Rev. Lett.* **112**, 036601 (2014).
- [36] N. Ru, R. A. Borzi, A. Rost, A. P. Mackenzie, J. Laverock, S. B. Dugdale, and I. R. Fisher, *de Haas–van Alphen Oscillations in the Charge Density Wave Compound Lanthanum Tritelluride* LaTe₃, *Phys. Rev. B* **78**, 045123 (2008).
- [37] P. D. Grigoriev, A. A. Sinchenko, P. Lejay, A. Hadj-Azzem, J. Balay, O. Leynaud, V. N. Zverev, and P. Monceau, *Bilayer Splitting versus Fermi-Surface Warping as an Origin of Slow Oscillations of In-Plane Magnetoresistance in Rare-Earth Tritellurides*, *Eur. Phys. J. B* **89**, 151 (2016).
- [38] This assumption is not *a priori* obvious. While the difference in the *a* and *c* lattice parameters is small, and can in principle be compensated for by an externally induced strain of equal magnitude, the material would nevertheless remain fundamentally orthorhombic due to the glide plane (a nonsymmorphic symmetry element that cannot be changed or removed solely by strain). The fact that our observations reveal a rotation of the CDW wave vector indicates that the glide plane is not crucial in establishing the direction of the CDW wave vector.
- [39] Analogous stress and strain terms can be defined in the orthorhombic reference frame as well [e.g., $\epsilon_A = (\epsilon_{cc} - \epsilon_{aa})/2$], however it should be noted that the subscripts *A* and *S* do not formally correspond to antisymmetric and symmetric strains; in the absence of tetragonal symmetry, these are no longer independent basis functions for different irreducible representations of the point group.
- [40] H. Yao, J. A. Robertson, E.-A. Kim, and S. A. Kivelson, *Theory of Stripes in Quasi-Two-Dimensional Rare-Earth Tellurides*, *Phys. Rev. B* **74**, 245126 (2006).
- [41] A. Fang, J. A. W. Straquadine, I. R. Fisher, S. A. Kivelson, and A. Kapitulnik, *Disorder-Induced Suppression of Charge Density Wave Order: STM Study of Pd-Intercalated ErTe₃*, *Phys. Rev. B* **100**, 235446 (2019).
- [42] A. T. Hristov, J. C. Palmstrom, J. A. W. Straquadine, T. A. Merz, H. Y. Hwang, and I. R. Fisher, *Measurement of Elastoresistivity at Finite Frequency by Amplitude Demodulation*, *Rev. Sci. Instrum.* **89**, 103901 (2018).
- [43] A. T. Hristov, M. S. Ikeda, J. C. Palmstrom, and I. R. Fisher, *Signatures of Anelastic Domain Relaxation in Ba(Fe_{1-x}Co_x)₂As₂ Investigated by Mechanical Modulation of Resistivity*, arXiv:1903.04732.
- [44] M. S. Ikeda, J. A. W. Straquadine, A. T. Hristov, T. Worasaran, J. C. Palmstrom, M. Sorensen, P. Walmsley, and I. R. Fisher, *AC Elastocaloric Effect as a Probe for Thermodynamic Signatures of Continuous Phase Transitions*, *Rev. Sci. Instrum.* **90**, 083902 (2019).
- [45] M. Saint-Paul, C. Guttin, P. Lejay, G. Remenyi, O. Leynaud, and P. Monceau, *Elastic Anomalies at the Charge Density Wave Transition in TbTe₃*, *Solid State Commun.* **233**, 24 (2016).
- [46] M. Saint-Paul, G. Remenyi, C. Guttin, P. Lejay, and P. Monceau, *Thermodynamic and Critical Properties of the Charge Density Wave System ErTe₃*, *Physica (Amsterdam)* **504B**, 39 (2017).
- [47] A. Sacchetti, C. L. Condon, S. N. Gvasaliya, F. Pfuner, M. Lavagnini, M. Baldini, M. F. Toney, M. Merlini, M. Hanfland, J. Mesot, J.-H. Chu, I. R. Fisher, P. Postorino, and L. Degiorgi, *Pressure-Induced Quenching of the Charge-Density-Wave State in Rare-Earth Tritellurides Observed by X-Ray Diffraction*, *Phys. Rev. B* **79**, 201101(R) (2009).
- [48] P. Walmsley and I. R. Fisher, *Determination of the Resistivity Anisotropy of Orthorhombic Materials via Transverse Resistivity Measurements*, *Rev. Sci. Instrum.* **88**, 043901 (2017).
- [49] A. Kogar *et al.*, *Light-Induced Charge Density Wave in LaTe₃*, *Nat. Phys.* **16**, 159 (2020).
- [50] The normalizing resistivity ρ_0 is usually taken as the geometric mean of the relevant resistivity tensor components at zero strain [51]. However, due to large ($\approx 20\%$) changes in the resistivity as shown in Fig. 6(b), we elect instead to normalize by the simultaneously measured average resistivity. This allows us to present our data without making any ancillary measurements or extrapolations.
- [51] M. C. Shapiro, P. Hlobil, A. T. Hristov, A. V. Maharaj, and I. R. Fisher, *Symmetry Constraints on the Elastoresistivity Tensor*, *Phys. Rev. B* **92**, 235147 (2015).
- [52] J.-H. Chu, H.-H. Kuo, J. G. Analytis, and I. R. Fisher, *Divergent Nematic Susceptibility in an Iron Arsenide Superconductor*, *Science* **337**, 710 (2012).
- [53] S. C. Riggs, M. Shapiro, A. V. Maharaj, S. Raghu, E. Bauer, R. Baumbach, P. Giraldo-Gallo, M. Wartenbe, and I. Fisher, *Evidence for a Nematic Component to the Hidden-Order Parameter in URu₂Si₂ from Differential Elastoresistance Measurements*, *Nat. Commun.* **6**, 6425 (2015).
- [54] H.-H. Kuo, J.-H. Chu, J. C. Palmstrom, S. A. Kivelson, and I. R. Fisher, *Ubiquitous Signatures of Nematic Quantum Criticality in Optimally Doped Fe-Based Superconductors*, *Science* **352**, 958 (2016).
- [55] E. W. Rosenberg, J.-H. Chu, J. P. C. Ruff, A. T. Hristov, and I. R. Fisher, *Divergence of the Quadrupole-Strain Susceptibility of the Electronic Nematic System YbRu₂Ge₂*, *Proc. Natl. Acad. Sci. U.S.A.* **116**, 7232 (2019).
- [56] M. Saint-Paul and P. Monceau, *Survey of the Thermodynamic Properties of the Charge Density Wave Systems*, *Adv. Condens. Matter Phys.* **2019**, 2138264 (2019).
- [57] M. Saint-Paul, C. Guttin, P. Lejay, O. Leynaud, and P. Monceau, *Elastic Properties of the Charge Density Wave System HoTe₃*, *Int. J. Mod. Phys. B* **32**, 1850249 (2018).
- [58] A. Zong, A. Kogar, Y.-Q. Bie, T. Rohwer, C. Lee, E. Baldini, E. Ergeçen, M. B. Yilmaz, B. Freelon, E. J. Sie, H. Zhou, J. Straquadine, P. Walmsley, P. E. Dolgirev, A. V. Rozhkov, I. R. Fisher, P. Jarillo-Herrero, B. V. Fine, and N. Gedik, *Evidence for Topological Defects in a Photoinduced Phase Transition*, *Nat. Phys.* **15**, 27 (2019).
- [59] A. Zong *et al.*, *Dynamical Slowing-Down in an Ultrafast Photoinduced Phase Transition*, *Phys. Rev. Lett.* **123**, 097601 (2019).
- [60] J. B. He, P. P. Wang, H. X. Yang, Y. J. Long, L. X. Zhao, C. Ma, M. Yang, D. M. Wang, X. C. Shangguan, M. Q. Xue, P. Zhang, Z. A. Ren, J. Q. Li, W. M. Liu, and G. F. Chen, *Superconductivity in Pd-Intercalated Charge-Density-Wave Rare Earth Poly-Tellurides RETe_n*, *Supercond. Sci. Technol.* **29**, 065018 (2016).
- [61] R. Lou, Y. Cai, Z. Liu, T. Qian, L. Zhao, Y. Li, K. Liu, Z. Han, D. Zhang, J. He, G. Chen, H. Ding, and S. Wang, *Interplay between Multiple Charge-Density Waves and the*

- Relationship with Superconductivity in Pd_xHoTe₃*, [Phys. Rev. B **93**, 115133 \(2016\)](#).
- [62] J. A. W. Straquadine, F. Weber, S. Rosenkranz, A. H. Said, and I. R. Fisher, *Suppression of Charge Density Wave Order by Disorder in Pd-Intercalated ErTe₃*, [Phys. Rev. B **99**, 235138 \(2019\)](#).
- [63] T. Giamarchi and P. Le Doussal, *Elastic Theory of Flux Lattices in the Presence of Weak Disorder*, [Phys. Rev. B **52**, 1242 \(1995\)](#).
- [64] G. W. Burns, M. G. Scroger, G. F. Strouse, M. C. Croarkin, and W. F. Guthrie, *Temperature-Electromotive Force Reference Functions and Tables for the Letter-Designated Thermocouple Types Based on the ITS-90*, National Institute of Standards Technology Monograph 175 (National Institute of Standards and Technology, Gaithersburg, MD, 1993).
- [65] M. S. Ikeda, T. Worasaran, J. C. Palmstrom, J. A. W. Straquadine, P. Walmsley, and I. R. Fisher, *Symmetric and Antisymmetric Strain as Continuous Tuning Parameters for Electronic Nematic Order*, [Phys. Rev. B **98**, 245133 \(2018\)](#).